Word Count: 10318

The role of graphite in the formation of unconformity-related uranium deposits of the Athabasca Basin, Canada: a case study of Raman spectroscopy of graphite from the world-class Phoenix uranium deposit

Revision 1 – clean copy

Hao Song[1,2], Guoxiang Chi[2,*], Kewen Wang[2], Zenghua Li[3], Kathryn M. Bethune[2], Eric G. Potter[4], and Yongxing Liu[5]

[1] Chengdu University of Technology, Chengdu, Sichuan 610059, China

[2] Department of Geology, University of Regina, Regina, Saskatchewan, Canada

[3] East China University of Technology, Nanchang, Jiangxi 330013, China

[4] Geological Survey of Canada, Ottawa, Ontario, Canada

[5] Denison Mines Corp., Saskatoon, Saskatchewan, S4S 0A2, Canada

*Corresponding author: guoxiang.chi@uregina.ca

Abstract

The unconformity-related uranium (URU) deposits in the Proterozoic Athabasca Basin (Canada) represent the richest and one of the most important uranium endowments in the world. Most of the URU deposits are associated with pre-existing graphitic basement faults that were reactivated after the formation of the basin. These graphite-rich structures have been widely used as a vector for exploration, but the nature of the association of the URU deposits with graphitic basement faults has been debated for over four decades. Proposed roles of graphite include: 1) as a direct reducing agent to reduce U^{6+} to U^{4+} and precipitate uraninite, 2) as a precursor of hydrocarbons (mainly CH_4) produced in situ or nearby and then used as a reducing agent for uraninite precipitation; 3) as a precursor of hydrocarbons produced at depth that were remobilized to the site of mineralization and acted as a reducing agent for uraninite precipitation; and 4) as a lubricant facilitating faulting and fluid flow that led to uranium mineralization. This paper uses the Phoenix uranium deposit in the southeastern Athabasca Basin as a case study to address these uncertainties. Petrographic studies indicate that there is no direct contact between graphite and uraninite at microscopic scales and the content of graphite in the graphitic metapelite along the ore-controlling WS Shear Zone does not show a systematic change with the distance from the unconformity surface. Raman spectroscopic studies of graphite suggest that the degree of structural disorder of graphite, expressed by various parameters related to the D bands and G band ratios, does not change systematically with the distance from the unconformity surface either. The minor

irregularities in these parameters near the unconformity are better explained by paleo-weathering related to the unconformity and/or diagenetic processes than by hydrothermal activity related to uranium mineralization. Based on these observations and interpretations, the role of graphite as an in situ reducing agent, either directly or as a provider of hydrocarbons, is discounted. It is proposed that hydrocarbons derived from graphite at depth, tapped by episodic reactivation or seismicity of the basement faults that was facilitated by graphite as a lubricant, were responsible for URU mineralization.

Key words: Raman spectroscopy, Graphite, Unconformity-related uranium (URU) deposits, Phoenix, Athabasca Basin

Introduction

The Proterozoic Athabasca Basin, located in northern Saskatchewan and Alberta, Canada (Fig. 1a), is known for its high-grade, large-tonnage uranium deposits located near the unconformity between the flat-lying sedimentary rocks in the basin and strongly deformed and metamorphosed rocks in the basement (Hoeve and Sibbald 1978; Jefferson et al., 2007; Kyser and Cuney 2015). These deposits, known as the unconformity-type or unconformity-related uranium (URU) deposits, are spatially associated with reactivated basement faults crosscutting and/or reversely displacing the unconformity surface, and most of the ore-controlling faults are developed in graphite-rich lithologies (Hoeve and Sibbald 1978; Jefferson et al. 2007; Kyser and Cuney 2015). As such, graphite has been generally considered to have played an important role, either directly or indirectly, in the formation of the URU deposits (Hoeve and Sibbald 1978; Hoeve and Quirt 1984; Kyser et al. 1989; Landais et al. 1993; Alexandre et al. 2005; Yeo and Potter 2010; Dargent et al.

66 2015; Potter and Wright 2015; Pascal et al. 2016a, b; Martz et al. 2017, 2019).
67 Consequently, graphite-rich zones interpreted from geophysical surveys, particularly
68 electromagnetic (EM) conductors, have been widely used to guide uranium exploration in
69 the Athabasca Basin for the last several decades (Hoeve and Sibbald 1978; Jefferson et al.
70 2007; Kerr 2010; Yeo and Potter 2010; Marlatt and Kyser 2011; Potter and Wright, 2015).
71 However, the nature of the relationship between graphite and URU mineralization
72 remains unclear, which affects the reliability of the exploration model.

73 In the original "diagenetic-hydrothermal' model of Hoeve and Sibbald (1978),
74 diagenetic fluids from the basin penetrated into the basement and reacted with graphite to
75 produce CH_4 and CO_2 that then flowed upward along facture zones toward the
76 unconformity surface, where U^{6+} carried by oxidizing basinal fluids was reduced by the
77 upwelling CH_4 and uraninite was precipitated. This model is supported by the presence of
78 blebs (or "buttons") of amorphous carbon or hydrocarbons (bitumen) in many of the
79 URU deposits (Hoeve and Sibbald 1978; Hoeve and Quirt 1984; Leventhal et al. 1987;
80 Kyser et al. 1989; Landais et al. 1993). However, based on comparison of C isotopes
81 between graphite and bitumen, Leventhal et al. (1987) and Kyser et al. (1989) suggested
82 that the bitumen found in the ores could not be derived from the nearby graphite.
83 Although the similarity in C isotopes between graphite and bitumen may be explained by
84 the formation of hydrocarbons through reaction between graphite and H_2 produced from
85 radiolysis of water (Dubessy et al. 1988), such a mechanism would not have operated
86 until there were significant amounts of uranium accumulation, i.e. post-mineralization
87 (Kyser et al. 1989). Wilson et al. (2007) also suggested that the bitumen associated with
88 URU deposits were introduced after mineralization, and inferred that the hydrocarbons

were sourced from the Douglas Formation in the Athabasca Basin based on biomarkers. McCready et al. (1999) and Annesley et al. (2001), on the other hand, presented petrographic and geochemical evidence suggesting that there is more than one generation of hydrocarbons in the URU deposits and that some were emplaced before mineralization, implying that hydrocarbons may have played a role in mineralization. None of the above-mentioned studies preclude the possibility that hydrocarbons derived from the basement at depth (instead of from graphite in the immediate host rocks) were the reducing agents responsible for URU mineralization (Dargent et al. 2015; Martz et al. 2017, 2019; Branquet et al. 2019). Fluid inclusions containing hydrocarbons (especially CH_4) as well as hydrogen gas (H_2) have been reported in many URU deposits (Derome et al. 2003; Pascal et al. 2016b; Richard 2017; Chi et al. 2018a; Martz et al. 2019), but the timing of entrapment of these gases relative to mineralization remains uncertain.

It has also been proposed that some U^{6+} in the ore-forming fluid may have been reduced to U^{4+} directly by graphite (Alexandre et al. 2005). However, this mechanism is not supported by a spatial association between graphite and uraninite at microscopic scales, as would be expected if graphite is used as reductant to precipitate uraninite (Yeo and Potter 2010). Furthermore, graphite has been shown to be a much less efficient reductant than H_2 and CH_4 (Dargent et al. 2015) and some URU deposits are hosted in non-graphitic lithologies, e.g., sericite-chlorite schist at the Centennial deposit, paragneiss at the Cluff Lake deposit, and quartzite and calc-meta-arkose at the Raven and Horseshoe deposit (Yeo and Potter 2010). Because of the controversies outlined above, some authors suggest that the main reducing agents for URU mineralization are neither graphite nor hydrocarbons derived from it, but rather non-carbon based species such as Fe^{2+} and H_2S

(Komninou and Sverjensky 1996; Yeo and Potter 2010; Ng et al. 2013), and graphite may simply serve as a lubricant facilitating basement fault reactivation and subsequent fluid flow (Kyser et al. 1989; Yeo and Potter 2010).

Regardless of the controversies regarding the origins of the hydrocarbons and their roles in URU mineralization, graphite in the vicinity of several URU deposits is more altered than graphite in the country rocks, as manifested by depletion or "consumption", corrosion and/or degradation of graphite at the site of mineralization (Hoeve and Sibbald 1978; Hoeve and Quirt 1984; Leventhal et al. 1987; Kyser et al. 1989; Wang et al. 1989; Landais et al. 1993; Yeo and Potter 2010; McCready et al. 1999; Annesley et al. 2001; Pascal et al. 2016a, b). However, the timing of these graphite alteration and destruction events are poorly constrained, ranging from pre-Athabasca Basin to post-mineralization (Dubessy et al. 1988; McCready et al. 1999; Annesley et al. 2001; Pascal et al. 2016a, b). Further studies of graphite from URU deposits, especially the temporal and spatial relationships between graphite alteration, hydrocarbon development and uranium mineralization are therefore warranted.

Raman spectroscopy has been widely used to address various Earth science problems (Dubessy et al. 2012; Chou and Wang 2017) and has been found particularly useful in studying the structure of graphite and related geological conditions (Landais et al. 1993; Beyssac et al. 2002, 2003; Lahfid et al. 2010; Martz et al. 2017). Crystalline graphite sensu stricto is made of ABAB stacking of graphene layers consisting of hexagonal unit cells constructed by carbon atoms, whereas the more general term 'graphitic carbon' include those that have amorphous-like or turbostratic structures (Beyssac and Rumble 2014). It has been well documented that the graphitization process

135 with increasing temperature is associated with increasing order of crystal structure
136 (Beyssac et al. 2002, 2003; Lahfid et al. 2010), and graphite can be degraded at lower
137 temperatures in the presence of fluids (Wang et al. 1989; Landais et al. 1993). Graphitic
138 carbons with different crystallinity or order of crystal structure have different Raman
139 spectroscopic characteristics (Beyssac et al. 2002, 2003; Lahfid et al. 2010), and therefore
140 Raman spectroscopic study may reveal the conditions of graphite formation and/or its
141 modification.

142 In this paper, we present a case study of graphite from the Phoenix uranium deposit
143 located in the southeastern Athabasca Basin (Fig. 1a; Kerr 2010; Wang 2016; Wang et al.
144 2018) in order to address the above-discussed problems regarding the roles of graphite in
145 URU mineralization. The Phoenix deposit has an estimated resource of 71.3 million
146 pounds of U_3O_8 at an average grade of 19.13 wt.% U_3O_8 (Roscoe 2014), making it one of
147 the richest and largest uranium deposits in the world (IAEA 2016). Graphite-bearing
148 samples with varying distances from the ore zone and/or unconformity were collected for
149 petrography and Raman spectroscopy. Different generations of graphite were recognized
150 and their relative timing with regard to other minerals were established based on
151 crosscutting relationships observed in the hand samples and thin sections. Minor fluid
152 inclusions associated with graphite were examined with microthermometry. The contents
153 of graphite in the rocks and various parameters indicating the graphite crystallinity were
154 estimated from the Raman spectra. Correlation of these parameters with the distance from
155 the ore zone and/or unconformity was then used to illustrate the role of graphite in the
156 formation of the Phoenix uranium deposit and broader association between graphite and
157 URU deposits in the Athabasca Basin. Finally, the results were integrated with previous

158 studies to illustrate how graphitic faults may have controlled fluid flow and the linkage
159 between ore fluids and the sources of reducing agents for URU mineralization.
160
161 **Regional and local geology**

162 The Paleoproterozoic to Mesoproterozoic Athabasca Basin contains mainly
163 siliciclastic rocks (the Athabasca Group) resting unconformably on Archean to
164 Paleoproterozoic basement (Ramaekers et al. 2007). The Athabasca Group is divided into
165 four unconformity-bounded sequences, which are, from bottom to top, the sandy to
166 conglomeratic Fair Point Formation (sequence 1), the quartz-arenitic Read, Smart and
167 Manitou Falls formations (sequence 2), the pebbly to sandy Lazenby Lake and mud-rich
168 Wolverine Point formations (sequence 3), and the pebbly to sandy and conglomeratic
169 Locker Lake, sandy Otherside, mud-rich Douglas, and dolomitic Carswell formations
170 (sequence 4) (Ramaekers et al. 2007). The western part of the basin is underlain by
171 basement rocks belonging to the Taltson magmatic zone and the Rae Province, and the
172 eastern part is underlain by the Hearne Province, which is bounded in the east by the
173 Trans-Hudson Orogen (Fig. 1a; Card et al. 2007). The Hearne Province consists of, from
174 west to east, the Virgin River, Mudjatik, Wollaston and Peter Lake domains (Fig. 1a). The
175 Wollaston Domain, which underlies the Phoenix deposit, is composed of
176 Paleoproterozoic metasedimentary rocks of the Wollaston Supergroup and Archean
177 granitoid gneisses, with minor amounts of mafic to felsic intrusions of unknown ages
178 (Annesley et al. 2005; Card et al. 2007; Yeo and Delaney 2007). Most of the basement

179 rocks were strongly deformed, forming tight to isoclinal northeast-trending doubly
180 plunging folds and thrust structures and subject to upper amphibolite- to lower
181 granulite-facies metamorphism during the Trans-Hudson orogeny (Annesley et al. 2005;
182 Card et al. 2007; Yeo and Delaney 2007).

183 The Phoenix uranium deposit is situated in the southeastern Athabasca Basin,
184 among a number of URU deposits distributed along the Mudjatik – Wollaston Transition
185 Zone (Fig. 1a). The mineralization occurs at the unconformity contact and is associated
186 with a basement fault zone called the WS Shear Zone (Figs. 1b and c). The sedimentary
187 rocks above the unconformity are conglomerates and sandstones of the Read Formation
188 and the overlying Manitou Falls Formation (Bosman and Korness 2007; Fig. 1c). The
189 basement rocks comprise graphitic and non-graphitic pelitic gneiss, semipelitic gneiss,
190 quartzite, and minor pegmatitic gneiss (Figs. 1b and c). Some of the pelitic units contain
191 garnet, cordierite and sillimanite indicative of upper amphibolite- to lower
192 granulite-facies metamorphism. The pelitic gneiss is referred to as metapelite in local
193 geological reports (e.g., Roscoe 2014; Figs. 1b and c), and the same term is adopted in
194 this paper. The WS Shear Zone strikes northeast, dips moderately to the southeast (Figs.
195 1b and c), and crosscuts the unconformity displaying a minor reverse offset. The fault
196 developed between graphitic metapelite and garnetiferous metapelite in the footwall, and
197 metapelite, pegmatitic rocks and garnetiferous metapelite in the hanging wall (Figs. 1b
198 and c). A massive quartzite body, characterized by a prominent ridge of the unconformity
199 surface (basement high), is situated to the west of the garnetiferous metapelite in the

200 footwall (Figs. 1b and c). It is worth noting that, in contrast to the conventional
201 interpretation of quartzite and graphitic metapelite as derived from metamorphism of
202 sedimentary rocks, the quartzite and the graphite in the graphitic metapelite and the study
203 area have been alternatively interpreted as of hydrothermal origin (Card 2012, 2014;
204 Adlakha and Hattori 2021). In this paper, the terms of 'quartzite' and 'graphitic
205 metapelite' are used without considering their origins, as in Wang et al. (2018). The top 3
206 to 10 m of the basement rocks immediately below the unconformity were subject to
207 paleo-weathering (Kerr 2010).

208 The orebodies of the Phoenix deposit occur as shallowly dipping lenses mostly
209 hosted by the lowermost Athabasca Group above the unconformity, underlain by
210 graphitic metapelite and the WS Shear Zone (Figs. 1c, 2a). Parts of the orebodies extend
211 into the basement for a few meters, and minor discontinuous, thin ore lenses are
212 developed along steeply dipping subsidiary faults associated with the WS Shear Zone.
213 The ores are composed of uraninite and variable amounts of kaolinite, tourmaline
214 (magnesio-foitite), illite and minor sulfides (mainly pyrite) (Wang et al. 2018). The
215 mineralized zones are surrounded by a desilicification and clay alteration halo (Fig. 2a)
216 characterized by disintegration of sandstone into loose grains and development of
217 pervasive clay-sized magnesio-foitite, kaolinite and illite, and minor amounts of chlorite.
218 Silicification, manifested as quartz cementation, especially drusy quartz filling fractures
219 and dissolution vugs, is widely developed in the sandstone outside the desilicification and
220 clay alteration halo, and drusy quartz is also locally developed in the basement (Wang et

al. 2018).

Sampling and analytical methods

A total of 45 samples containing graphite were collected from six drill cores (Fig. 1b and c; Table 1). Most samples are from the graphitic metapelite (Fig. 2b) of the WS Shear Zone, and some from the hanging wall and footwall, with variable distances from the orebodies and/or unconformity. A few samples were collected from a drill core (WR-412; Fig. 1b) that does not intersect the WS Shear Zone for comparison. In addition to graphitic metapelite, samples with quartz veins that contain graphite and crosscut graphitic metapelite (Fig. 2c) and pegmatite crosscut by graphite filling fractures (Fig. 2d) were also examined. The strategy of sampling was to identify different generations of graphite and to evaluate if there are systematic variations of properties and amounts of graphite dispersed in the graphitic metapelite along the WS Shear Zone with increasing distance from the unconformity surface or orebodies, by examining samples intersected by different drill cores at different depths. Samples collected from the hanging wall and footwall also allowed evaluation of lateral changes of graphite properties away from the graphitic fault zone.

The samples were made into polished thin sections for petrographic and Raman spectroscopic studies. Optical examination of polished thin sections was conducted on an Olympus BX51 petrographic microscope equipped with both transmitted and reflected light attachments. Different generations of graphite were identified and their relative

timing with respect to the paragenetic sequence established by Wang et al. (2018) was evaluated based petrographic observations. The content of graphite was estimated by moving the thin section randomly and point-counting 250 points (at the crosshair); only the graphite exposed on the surface (detected by reflected light) was counted for consistency.

Raman spectroscopic analyses were performed using a Renishaw RM2000 laser Raman spectrometer at the Geofluids Laboratory of the University of Regina. The excitation laser (Spectra-Physics) has a wavelength of 514.5 nm, the grating was set to 1,800 gr/mm, and the objective was ×50 with long working distance. Each generation of graphite was examined for their Raman spectroscopic characteristics, and the most abundant type of graphite that is dispersed in graphitic metapelite was studied on a 50 points per thin section basis. As the Raman spectra vary with the orientation of the crystal (Wang et al. 1989; Beyssac et al. 2002, 2003), the average of the 50 measurements were taken to represent the Raman characteristics of the individual sample, while the standard deviation reflects uncertainties as well as variation of crystal orientations. The laser was kept at low power (0.15 mW) to minimize the effect of heat induced by laser on graphite structure (Beyssac et al. 2003). Each spot was analyzed for 60 seconds (six acquisitions, 10 seconds each) in the range from 1000 to 3500 cm^{-1}, which covers all peaks of graphite.

The Raman spectra in the first-order region (1100 – 1800 cm^{-1}) are characterized by their peak location, intensity and area as well as several different combinations of

these parameters related to the degree of disorder of graphite crystal structure (Beyssac et al. 2002, 2003; Lahfid et al. 2010). There are two types of bands in this region: graphite (G) and defect (D) bands, the latter including four bands labelled D1 to D4 (Lahfid et al. 2010). The G band and D1 band have a prominent peak at 1580 – 1600 cm^{-1} and 1350 cm^{-1}, respectively, whereas D2 (1620 cm^{-1}) occurs as a right shoulder of the G band, D4 (1200 cm^{-1}) as a left shoulder of the D1 band, and D3 is superimposed on the trough between D1 and G (Lahfid et al. 2010). In perfectly crystalline graphite, only the G band is present (Beyssac et al. 2003). The areas of the individual bands were calculated using the Lorentzian peak-fitting profile (Lahfid et al. 2010) provided in the WiRE 3.4 software. The following parameters were used to describe the degree of disorder of graphite: 1) D1/G; 2) D/G, where D is the total of D bands; 3) RA1 = (D1+D4)/(D1+D2+D3+D4+G); and 4) R2 = D1 / (G+D1+D2), all as area ratios.

Results

Different generations of graphite and their petrographic characteristics

Four generations of graphite (Gr1 – Gr4) were recognized in the samples examined. Two of them (Gr1 and Gr3) were discernable from the hand samples (Fig. 2), and the other two (Gr2 and Gr4) were distinguished in thin sections (Fig. 3). Gr1 developed in the graphitic metapelite, as flakes oriented along the schistosity (Figs. 2b, c, 3a). Gr2 occurs as inclusions in quartz replacing or cementing metapelite (Fig. 3e). Gr3 developed within fractures in graphitic metapelite (Fig. 2b) and quartz veins (Fig. 2c) or pegmatitic

284 rocks (Fig. 2d) that crosscut graphitic metapelite. Gr3 is inferred to be later than Gr2 on
285 the basis that Gr3 crosscuts the quartz coeval with that enclosing Gr2. Gr4 is not actually
286 graphite, but rather amorphous carbonaceous matter that occurs in interstitial space in the
287 sandstones and as rare inclusions in drusy quartz (Fig. 3g). Among the four generations of
288 graphite, Gr1 is volumetrically the most abundant and best developed in the metapelite,
289 whereas the others are scattered and locally developed in various lithologies including
290 quartzite and pegmatites. No uraninite was found in the samples collected for graphite
291 study from the Phoenix deposit, so no petrographic relationships between graphite and
292 uraninite could be observed. However, microscopic and SEM-EDS examination of a
293 mineralized sample from Gryphon Zone (about 2.5 km west of Phoenix) indicates that
294 uraninite is not spatially associated with graphite; even when they occur close to each
295 other locally, they are rarely in contact (Fig. 3h).

296 Gr1 is dispersed in metapelite and is mostly flake-shaped or tabular (Fig. 3a), but
297 locally it shows more equant and irregular shapes (Fig. 3b) in samples close to the
298 unconformity. The width of Gr1 flakes vary from 10 to 200 μm. Under reflected light,
299 Gr1 grains have relatively high reflectance in the central part of individual crystals,
300 relatively low reflectance near the edge (Fig. 3c), and the average reflectance appears to
301 be relatively low for crystals in samples close to the unconformity. Micron- to
302 sub-micron-sized pits (micro-pits), similar to the “hollow points” reported for the Cigar
303 Lake uranium deposit by Wang et al. (1989), are locally developed in Gr1 in samples
304 close to the unconformity (Fig. 3d). Gr2 is round-shaped and occurs as aggregates or

individual inclusions (blebs) enclosed within quartz that replaced graphitic metapelite (Fig. 3e). The size of individual grains or blebs range from a few to tens of microns. The reflectance is relatively high (even under quartz) and fairly homogeneous (Fig. 3e insert). Gr3 shares some similarities with Gr1 but it is generally more equant-shaped, coarser-grained and of higher reflectance than Gr1 (Fig. 3 f). It occurs in microfractures or interstitial space, and is commonly associated with pyrite (Fig. 3f). Gr4 in growth zones in drusy quartz (Fig. 3g) is rare and characterized by irregular shapes and very low reflectance.

Raman spectroscopic characteristics of different generations of graphite

The Raman spectra of Gr1 grains are characterized by a prominent G band at 1582 cm^{-1}, with or without a D1 band at 1356 cm^{-1} and a D2 band at 1620 cm^{-1} (Fig. 4a), suggesting variable degrees of structural disorder. Gr1 that has micro-pits shows more intense D bands than Gr1 without micro-pits (Fig. 4b), and Gr1 within the micro-pits shows stronger D bands than Gr1 outside the micro-pits (Fig. 4c). All Gr2 grains show a sharp G band with no D bands in the first order region (Fig. 4d), indicating a very high degree of structural order. Gr3 mostly has similar Raman spectra as Gr2, i.e., only the G band and not D bands in the first order region, but some show a minor D1 band (Fig. 4e). The Raman spectra of Gr4 are characterized by a dominant D1 band at ~1350 cm^{-1} and a broad band combining G and significant D2 at ~1600 cm^{-1} (Fig. 4f), and some spectra also show a broad D3 band at 1500 cm^{-1}, all indicating a very high degree of structural disorder.

326 **Fluid inclusions associated with Gr2**

327 Fluid inclusions are locally associated with Gr2 blebs (Fig. 5). Some blebs contain
328 a visible fluid phase composed of CO_2, CH_4 and N_2 as detected by Raman spectroscopy
329 (Fig. 5a), and others contain CH_4 and N_2 even though no fluid phase was discernable (Fig.
330 5b). In some healed fractures, Gr2 blebs occur with CH_4 and aqueous inclusions, forming
331 a fluid inclusion assemblage (FIA; Goldstein and Reynolds 1994) (Fig. 5c). An aqueous
332 liquid is attached to some of the Gr2 blebs (Fig. 5c). The CH_4 inclusions are monophase
333 at room temperature and nucleated a liquid phase when cooled to temperatures between
334 -100 and -170 °C (Fig. 5d). In one FIA, the CH_4 inclusions show homogenization (to
335 vapor) temperatures from -165.0 to -120.4 °C (n = 22), and the aqueous inclusions have
336 ice-melting temperatures from -0.9 to -2.6 °C, with calculated salinities from 1.8 to 4.3
337 wt.% NaCl equivalent, and homogenization (to liquid) temperatures from 106 to 276 °C
338 (n = 9). In another FIA, the CH_4 inclusions show homogenization (to vapor) temperatures
339 from -113.1 to -98.5 °C (n = 5). Fluid pressures estimated from the isochores of the CH_4
340 inclusions, calculated with the equation of Setzmann and Wagner (1991) in the FLUIDS
341 software of Bakker (2003), range from 3 to 140 bars for the temperature range from 106
342 to 276 °C.

343 **Graphite abundance and spatial variation**

344 The volumetric abundance of graphite (mainly Gr1) in the samples studied, based on
345 250 counts in each thin section, range from 0 to 9.2% (n = 45; Table 1). The samples are
346 divided into three types: 1) graphitic metapelite in the WS Shear Zone; 2) hanging wall and

347 footwall of the WS Shear Zone; and 3) drill core (WR-412) that is located ~500 m away
348 from the WS Shear Zone (Fig. 1b). The diagrams correlating the abundance of graphite
349 with the vertical distance of the sample from the unconformity surface (Fig. 6) show that
350 there is no systematic variation over a distance of ~200 m (Fig. 6a). There is a trend of
351 decreasing graphite abundance toward the unconformity in the top 10 – 50 m of the
352 basement, but no trends of graphite abundance with depth are discernable if the top 10 m
353 (shaded area in Fig. 6) is excluded.

354 **Degree of order of graphite (Gr1) structure and spatial variation**

355 The parameters of Raman spectra of graphite (Gr1) that indicate the degree of
356 crystal structural disorder, i.e., D1/G, D/G, RA1 = (D1+D4) / (D1+D2+D3+D4+G), and
357 R2 = D1 / (G+D1+D2) (Table 1; Supplementary Table 1), are plotted against the distance
358 from the unconformity surface (Fig. 7; Supplementary Figs. 1 – 4). These parameters
359 show similar patterns with regard to depth, where no significant change with depth is
360 observed except more scattered distribution in the top ~25 meters below the
361 unconformity (Fig. 7), and no significant change is observed in individual drill cores,
362 especially if the top 10 meters below the unconformity are excluded (Fig. 8). The samples
363 from the hanging wall or footwall, and those in drill core WR-412 far away from the WS
364 Shear Zone, exhibit the same trend as those in the WS Shear Zone (Figs. 7 and 8).

365 Using the graphite thermometer of Beyssac et al. (2002) (T (^{o}C) = -445 R2 + 641),
366 where R2= D1 / (G+D1+D2), the formation temperatures of Gr1 graphite were calculated
367 to be from 516 to 613 ^{o}C (Table 1). There is no discernable trend of temperatures with

368 depth, except an abrupt drop in calculated temperatures in the top ~25 meters below the
369 unconformity (Fig. 9a). For individual drill cores, there is no systematic change in
370 temperatures with depth, especially if the top 10 m below the unconformity is excluded
371 (Fig. 9b-f).

372

373 **Discussion**

374 There is no dispute that graphite-rich fault zones play an important role in the
375 formation of most URU deposits, but the role of graphite during uranium mineralization
376 is still unclear. Roles of graphite can be divided into two categories: chemical and
377 mechanical. In the first category, graphite or hydrocarbons derived from graphite served
378 as the reducing agents to reduce U^{6+} to U^{4+} and precipitate uraninite (Hoeve and Sibbald
379 1978; Hoeve and Quirt 1984; Landais et al. 1993; Alexandre et al. 2005; Dargent et al.
380 2015; Pascal et al. 2016a, b; Martz et al. 2017, 2019; Branquet et al. 2019). In the second
381 category, graphite played the role of a lubricant that facilitated fault reactivation and thus
382 controlled channeling of ore-forming fluids (Kyser et al. 1989; Yeo and Potter 2010).

383 The chemical roles of graphite can be further divided into three scenarios: 1)
384 graphite was directly used as a reducing agent to precipitate uraninite (Alexandre et al.
385 2005); 2) hydrocarbons (especially CH_4) derived from interactions between graphite and
386 aqueous fluids, which took place at or near the site of, and coeval with, uranium
387 mineralization, served as reducing agents to precipitate uraninite (Hoeve and Sibbald
388 1978; Hoeve and Quirt 1984; Landais et al. 1993; Pascal et al. 2016a,b); and 3) CH_4

produced from graphite – aqueous fluid reactions at depth prior to uranium mineralization was delivered to the site of mineralization and served as a reducing agent to precipitate uraninite (Dargent et al. 2015; Martz et al. 2017, 2019; Branquet et al. 2019). These three scenarios are discussed below in light of the results obtained in this study. Note, although these scenarios emphasize the chemical roles of graphite, they are not necessarily against the notion that graphite also played a mechanical role in facilitating faulting.

As discussed in Yeo and Potter (2010), the hypothesis that graphite was directly used as a reducing agent in uranium mineralization is generally not supported by microscopic observations, i.e., uraninite was not intimately associated with graphite at a micro-scale. This is also the case for the Phoenix uranium deposit. First of all, like other sandstone-hosted (or egress style) URU deposits, the orebodies in the Phoenix deposit overlie, rather than replace, graphite-rich basement rocks (Fig. 2a), thus excluding the possibility of graphite being used directly as a reducing agent at a deposit scale. Secondly, like in other URU deposits, no crystal-scale replacement of graphite by uraninite was observed even when graphitic metapelite was locally mineralized (Fig. 3h). Therefore, textural observations presented in this study do not support the hypothesis that graphite served as a reducing agent for URU mineralization.

Additionally, the results from this study do not support the breakdown of graphite at the site of mineralization, because the decrease of graphite abundance towards the unconformity is unclear and unrelated to uranium mineralization. There is no clear trend of decreasing graphite content toward the orebodies except perhaps the top 10 m below

410 the unconformity (Fig. 6). The decrease of graphite content near the sites of mineralization
411 have been reported in many URU deposits, which has been used as an argument that in-situ
412 graphite consumption is related to uranium mineralization (Hoeve and Sibbald 1978;
413 Hoeve and Quirt 1984; Landais et al. 1993). However, the possibility that the graphite
414 consumption was caused by weathering during formation of the unconformity, i.e., before
415 the formation of the Athabasca Basin and uranium mineralization (Pascal et al. 2016a, b),
416 cannot discounted. Furthermore, the uppermost part of the basement have been overprinted
417 by diagenetic fluids of the Athabasca Basin (Adlakha et al. 2014), which may have also
418 contributed to consumption of the graphite. This scenario of paleo-weathering +/-
419 diagenetic overprint is supported by the observation that samples from the hanging wall
420 and footwall of the mineralized WS Shear Zone as well as at a locality ~500 m away from
421 the WS Shear Zone also show a decrease of graphite content near the unconformity (Fig. 6).
422 The dissolution features of graphite (Gr1), including corroded grains (Fig. 3b) and
423 micro-pits (Fig. 3d), may have been produced during the paleo-weathering and diagenetic
424 processes. The slight increase of the degree of structural disorder of graphite near the
425 unconformity, as indicated by Raman spectra parameters (Figs. 7 and 8) and calculated
426 temperatures (Fig. 9), can also be explained by paleo-weathering and diagenetic processes.
427 Although minor contribution of hydrocarbons derived from in situ graphite –
428 aqueous solution reaction to uranium mineralization depicted in the conventional
429 diagenetic-hydrothermal model (Hoeve and Sibbald 1978; Hoeve and Quirt 1984;
430 Landais et al. 1993) cannot be entirely excluded, the reducing agents for uranium

mineralization at Phoenix were possibly derived from external sources. The overall reducing environment in the basement is favorable for development of various reducing species in the basement fluids, including CH_4, H_2, Fe^{2+}, CO, and H_2S (Dargent et al. 2015). For sandstone-hosted URU deposits including the Phoenix deposit, Fe^{2+} cannot be an important reducing agent for uranium mineralization, because the alteration halo associated with mineralization is characterized by bleaching (dissolution of hematite in the sandstone) rather than reddening (precipitation of hematite). The more likely reducing agents involved in the URU mineralization are CH_4, H_2, and C_2H_6 as detected in fluid inclusions associated with URU deposits (Dargent et al. 2015; Richard 2017). Although these reducing agents may be pervasive in the basement, they are more likely to develop and accumulate in graphite-rich zones, forming a gas reservoir without a physical boundary (Fig. 10). Such a reservoir may be sustained by the overall low permeability of the surrounding rocks and continuous generation of gases through chemical reactions such as: $2C + 2H_2O = CH_4 + CO_2$; $C + 2H_2O = CO_2 + 2H_2$; and $CO_2 + 4H_2 = CH_4 + 2H_2O$ (Dargent et al. 2015).

It is well understood that methane can be generated from cracking of larger hydrocarbons at elevated temperatures and pressures through thermogenic processes (Vanderbroucke and Largeau 2007). Significant amounts of methane may be formed during the prograde metamorphism (1840 – 1805 Ma) (Martz et al. 2017) and formation of the flaky graphite (Gr1). The maximum temperature at this time was estimated to be ~ 610 ^{o}C (Table 1), which is similar to that estimated by Martz et al. (2017) for metamorphic

graphite at the Cigar Lake uranium deposit (~ 640 °C) but lower than the peak metamorphism condition of the Trans-Hudson orogeny (~ 800 °C, Martz et al. 2017; ~ 875 °C, Adlakha and Hattori 2021). The formation of Gr2, and probably Gr3, likely took place at higher temperatures, as reflected by the almost perfect Raman G band without any D bands in Gr2 (Fig. 4d). A similar occurrence of graphite (as inclusions in quartz and tourmaline) has been reported in the basement rocks of the McArthur River deposit (Adlakha et al. 2000), and the age of the rutile associated with the graphite has been constrained to 1723 +/-12 ~ 1750 +/-5 Ma, which is linked with a thermal event related to asthenospheric upwelling (Adlakha and Hattori 2021). Large amounts of methane may have been produced during this period of time, as testified by the occurrence of CH_4 inclusions with Gr2 (Fig. 5). However, the very low density of the methane inclusions, as suggested by the homogenization into the vapor phase (Fig. 5d), the low homogenization temperatures of the associated aqueous inclusions (106 to 276 °C), and the low pressures calculated from these inclusions (3 to 140 bars), all suggest entrapment of these inclusions at shallow depths. The coexistence of methane and aqueous inclusions within individual FIAs (Fig. 5c) suggests fluid immiscibility, and therefore the homogenization temperatures of the aqueous inclusions may represent the tapping temperatures, and the calculated fluid pressures at these temperatures represent the trapping pressure. Even if the trapping temperatures were higher than the homogenization temperatures of the aqueous inclusions, the calculated fluid pressures would still be low due to the low density of the CH_4 inclusions. Similar P-T conditions have also been obtained from CH_4 inclusions in other

473 URU deposits (Pascal et al. 2016b). A possible explanation for the apparent contradiction
474 between the high temperature suggested by Gr2 and the low temperature and pressure
475 suggested by the associated fluid inclusions is that the microfractures that host Gr2 and
476 fluid inclusions were reopened during the exhumation process. This hypothesis is
477 supported by variation of homogenization temperatures of CH_4 and aqueous inclusions
478 within the same FIAs. Low salinities of the aqueous inclusions (1.8 to 4.3 wt.% NaCl
479 equivalent), which are in contrast to the basinal brines from the Athabasca Basin (Chu
480 and Chi 2016; Richard et al. 2016), suggests that this reopening did not happen during or
481 after development of brines in the basin, perhaps during the exhumation process of the
482 basement rocks before the formation of the Athabasca Basin.

483 For the reducing gases generated at depth in the basement to participate in the
484 formation of URU deposits, they need to be delivered to the site of mineralization near the
485 unconformity, and the reactivated basement faults likely played a critical role. The WS
486 Shear Zone in the Phoenix deposit, like most of the basement faults that host URU deposits,
487 displays features indicating reverse faulting after the formation of the Athabasca Basin
488 (Kerr 2010; Roscoe 2014; Wang et al. 2018). Such reverse reactivation of the basement
489 faults has been shown to be able to drive egress fluid flow from the basement toward the
490 unconformity (Li et al. 2017, 2018). During episodic reactivation of the basement faults,
491 reducing gases may have been released from the reservoir at depth. In addition to providing
492 the driving force for fluid flow during faulting (seismicity), the tectonic process also
493 enhances the permeabilities of the fault zones, which in turn enhances fluid convection

494 during the interseismic periods (Branquet et al. 2019; Li et al. 2020). Thus, formation of
495 URU deposits may be related to alternating deformation-driven flow and fluid convection
496 due to episodic seismicity (Fig. 10).

497 The environment in which the seismicity, as well as the fluid flow and mineralization
498 events, took place is still controversial. Many authors consider that URU mineralization
499 took place at depths of 5 – 6 km, and fluid pressure fluctuated between lithostatic and
500 hydrostatic regimes (e.g., Pagel 1975; Richard et al. 2016; Martz et al. 2017, 2019;
501 Branquet et al. 2019), whereas others suggest that the mineralization likely took place at
502 depths of ~3 km, and fluid pressure fluctuated between hydrostatic and sub-hydrostatic
503 regimes (Chi et al. 2018b; Wang et al. 2018). We favor the latter model based on the
504 inference of hydrostatic pressure regime in the Athabasca Basin due to dominance of
505 sandstones (Chi et al. 2013), geochrono-stratigraphic constraints (Chi et al. 2018b), and
506 sub-hydrostatic fluid pressures indicated by fluid inclusions (Rabiei et al. 2017, 2021;
507 Wang et al. 2018). According to the first model, the reactivation of the basement faults
508 may be compared to the fault-valve model of Sibson et al. (1988), whereas the second is
509 similar to the seismic suction pump model of Sibson (1987, 2001). We propose here that
510 the seismicity was triggered at the base of the basement faults, which was ~ 5 km below the
511 unconformity, where the deformation regime was transitional between brittle and ductile,
512 and fluid pressure was normally lithostatic and dropped to hydrostatic during fracturing, as
513 depicted by the fault-valve model (Sibson et al. 1988). At the upper tip of the fault near the
514 unconformity surface, where URU mineralization took place, the fluid pressure was

515 normally hydrostatic and dropped to sub-hydrostatic during seismic fracturing, causing
516 instant fluid boiling and drainage of basement-derived fluids rich in reducing gases. The
517 upward flow of basement fluids and gases would continue after these seismic events,
518 providing reducing agents for uranium mineralization in the inter-seismic periods (Fig.
519 10).

520 Based on the above discussions, the nature of the association of URU mineralization
521 and reactivated graphite-rich basement faults may be envisaged as dual roles of graphite:
522 on one hand, graphite provided the most important ingredient for making reducing gases
523 (especially CH_4 and H_2) at depth, and on the other hand, the reactivation of the basement
524 faults, enhanced by graphite as a lubricant, helped deliver reducing gases to the site of
525 mineralization. The model proposed here is different from the conventional
526 diagenetic-hydrothermal model (Hoeve and Sibbald 1978; Hoeve and Quirt 1984) in that
527 the generation of hydrocarbons required for uranium mineralization did not take place at or
528 near the site of mineralization, but rather at depth (> 5 km below the unconformity). In
529 addition, hydrocarbons were not produced at the time of mineralization, but were generated
530 mainly during metamorphism and subsequent fluid-rock reactions and then stored in and
531 around the source rocks. Our model is also different from those that assumed great burial
532 depths of the unconformity during mineralization (5 – 6 km; Richard et al. 2016; Martz et
533 al. 2017, 2019; Branquet et al. 2019), even though both suggest that the reducing gases
534 were derived from depths instead of in situ. Our combined fault-valve and suction pump
535 model (Fig. 10), with the reactivated basement faults connecting the sites of mineralization

with the reservoir of reducing gases, is a plausible explanation of the genetic link between URU deposits and graphitic basement faults.

Implications

This study uses Raman spectroscopy to examine the temporal and spatial variation of graphite along a reactivated basement fault controlling the Phoenix URU deposit in the Athabasca Basin. The purpose was to evaluate the role of graphite in URU mineralization, which has been investigated for over four decades and remains debated. The results indicate that although URU mineralization is spatially associated with underlying graphitic lithologies in the basement, the graphite in the immediate host rocks did not play a major role in uranium mineralization, either directly as a reducing agent, or as precursor of hydrocarbons. Instead, hydrocarbons generated from graphite – fluid reactions at depth were likely the source of reducing agents for the uranium mineralization. These reducing gases were tapped during fault reactivation, which was facilitated by graphite as a lubricant, and delivered from the reservoir at depth to the site of mineralization.

Raman spectroscopy has been previously applied to the study of graphite associated with URU deposits, but the great number of measurements from spatially spread out samples in this study provides new insights on the role of graphite. This case study serves as an example of how a proven technology can tackle some long-standing scientific problems using a different approach. The model and method developed in this study are applicable to other studies investigating the hydrodynamic link between shallow, hydrostatic-dominated

and deep-seated, lithostatic-dominated environments. The conditions and geological processes (both mechanical and chemical) in such transitional environments are of broad interest to geoscientists working in the general fields of tectonics, mineral systems and seismology.

Acknowledgements

This study is financially supported by an NSERC-Discovery grant (to Chi) and the Geological Survey of Canada Targeted Geoscience Initiative Phase 4 (TGI-4) program. Denison Mines Corp. is acknowledged for allowing core logging and sampling and field accommodation. Clark Gamelin and Chad Sorba from Denison Mines and Morteza Rabiei are thanked for assistance in field work. We thank Dr. Erin Adlakha and an anonymous reviewer for detailed and constructive reviews and Associate Editor Dr. Yassir Abdu for editorial handling, which all helped improve the paper.

References

Adlakha, E., and Hattori, K. (2021) Thermotectonic events recorded by U-Pb geochronology and Zr-in-rutile thermometry of Ti oxides in basement rocks along the P2 fault, eastern Athabasca Basin, Saskatchewan, Canada. Geological Society of America Bulletin, 2021, https://doi.org/10.1130/B35820.1

Adlakha, E.E., Hattori, K., Zaluksi, G., Kotzer, T., and Potter, E.G. (2014) Alteration within the basement rocks associated with the P2 fault and the McArthur River

578 uranium deposit, Athabasca Basin. Geological Survey of Canada, Open File 7462, 35
579 p. doi:10.4095/293364

580 Adlakha, E., Hattori, K., Kerr, M., and Boucher, B. (2020) The origin of Ti-oxide
581 minerals below and within the eastern Athabasca Basin, Canada. The American
582 Mineralogist, 105, 1875–1888.

583 Alexandre, P., Kyser, K., Polito, P., and Thomas, D. (2005) Alteration mineralogy and
584 stable isotope geochemistry of paleoproterozoic basement hosted unconformity-type
585 uranium deposits in the Athabasca Basin, Canada. Economic Geology, 100,
586 1547–1563.

587 Annesley, I.R., Madore, C., and Cutler, J. (2001) Synchrotron X-ray analysis of granitic
588 pelitic gneisses in the vicinity of unconformity-type uranium mineralization. Summary
589 of Investigation, Saskatchewan Geological Survey, Sask Energy Mines, Misc. Rep., 2,
590 132–140.

591 Annesley, I.R., Madore, C., and Portella, P. (2005) Geology and thermotectonic evolution
592 of the western margin of the Trans-Hudson Orogen: Evidence from the eastern
593 sub-Athabasca basement, Saskatchewan. Canadian Journal of Earth Sciences, 42,
594 573–597.

595 Arseneau, G., and Revering, C. (2010) Technical Report on the Phoenix Deposit (zones
596 A & B)-Wheeler River project, Eastern Athabasca Basin, Northern Saskatchewan,
597 Canada, NI 43-101 Report.

598 Bakker, R.J. (2003) Package FLUIDS 1. Computer programs for analysis of fluid
599 inclusion data and for modelling bulk fluid properties. Chemical Geology, 194, 3–23.
600 Beyssac, O., and Rumble, D. (2014) Graphitic carbon: a ubiquitous, diverse and useful
601 geomatieral. Elements, 10, 415–420.
602 Beyssac, O., Goffé, B., Chopin, C., and Rouzaud, J. (2002) Raman spectra of
603 carbonaceous material in metasediments: A new geothermometer. Journal of
604 Metamorphic Geology, 20, 859–871.
605 Beyssac, O., Goffé, B., Petitet, J., Froigneux, E., Moreau, M., and Rouzaud, J. (2003) On
606 the characterization of disordered and heterogeneous carbonaceous materials by
607 Raman spectroscopy. Spectrochimica Acta Part A: Molecular and Biomolecular
608 Spectroscopy, 59, 2267–2276.
609 Branquet, Y., Boulvais, P., Mercadier, J., Ledru, P., and Khairallah, C. (2019)
610 Methaniferous active faults and seismic cycle in the genesis of the Athabasca giant U
611 deposits: conceptual and numerical investigation. Proceedings of the 15th Biennial
612 SGA Meeting, August 27-30, 2019, Glasgow, Scotland, V1, 52–55.
613 Card, C.D. (2012) The origins of anomalously graphitic rocks and quartzite ridges in the
614 basement to the southeastern Athabasca Basin; in Summary of Investigations 2012,
615 Volume 2, Saskatchewan Geological Survey, Sask. Ministry of the Economy, Misc.
616 Rep., 6, 15 p.
617 Card, C. (2014) Altered pelitic gneisses and associated “quartzite ridges” beneath the
618 southeastern Athabasca Basin: alteration facies and their relationship to uranium

619 deposits along the Wollaston-Mudjatik transition; in Summary of Investigations 2013,
620 Volume 2, Saskatchewan Geological Survey, Sask. Ministry of the Economy, Misc.
621 Rep. 2013-4.2, Paper A-4, 23p.

622 Card, C.D., Pana, D., Portella, P., Thomas, D.J., and Annesley, I.R. (2007) Basement
623 rocks to the Athabasca Basin, Saskatchewan and Alberta. Bulletin of the Geological
624 Survey of Canada, 588, 69–88.

625 Chi, G., Bosman, S., and Card, C. (2013) Numerical modeling of fluid pressure regime in
626 the Athabasca basin and implications for fluid flow models related to the
627 unconformity-type uranium mineralization. Journal of Geochemical Exploration, 125,
628 8–19.

629 Chi, G., Blamey, N.J.F., Rabiei, M., and Normand, N. (2018a) Hydrothermal REE
630 (xenotime) mineralization at Maw Zone, Athabasca Basin, Canada, and its relationship
631 with unconformity-related uranium deposits – A reply. Economic Geology, 113,
632 998–999.

633 Chi, G., Li, Z., Chu, H., Bethune, K.M., Quirt, D.H., Ledru, P., Normand, C., Card, C.,
634 Bosman, S., Davis, W.J., and Potter, E.G. (2018b) A shallow-burial mineralization
635 model for the unconformity-related uranium deposits in the Athabasca Basin.
636 Economic Geology, 113, 1209–1217.

637 Chou, I.-M., and Wang, A. (2017) Application of laser Raman micro-analyses to Earth
638 and planetary materials. Journal of Asian Earth Sciences, 145, 309–333.

639 Chu, H., and Chi, G. (2016) Thermal profiles inferred from fluid inclusion and illite
640 geothermometry from sandstone of the Athabasca basin: Implications for fluid flow
641 and unconformity-related uranium mineralization. Ore Geology Review, 75, 284–303.
642 Dargent M., Truche, L., Dubessy, J., Bessaque, G., and Marmier, H. (2015) Reduction
643 kinetics of aqueous U(VI) in acidic chloride brines to uraninite by methane, hydrogen
644 or C-graphite under hydrothermal conditions: Implications for the genesis of
645 unconformity-related uranium ore deposits. Geochimica et Cosmochimica Acta, 167,
646 11–26.
647 Derome, D., Cathelineau, M., Lhomme, T., and Cuney, M. (2003) Fluid inclusion
648 evidence of the differential migration of H2 and 02 in the McArthur River
649 unconformity-type uranium deposit (Saskatchewan, Canada). Possible role on post-ore
650 modifications of the host rocks. Journal of Geochemical Exploration, 78–79, 525–530.
651 Dubessy, J., Caumon, M.-C., and Rull, F. (2012) Raman spectroscopy applied to Earth
652 sciences and cultural heritage. EMU Notes in Mineralogy, 12, Cambrian Printers,
653 Aberystwyth, UK, pp. 1–504.
654 Dubessy J., Pagel M., Beny J.M., Christensen H., Hickel B., Kosztolanyi C., and Poty B.
655 (1988) Radiolysis evidenced by H_2–O_2 and H_2-bearing fluid inclusions in three
656 uranium deposits. Geochimica et Cosmochimica Acta, 52, 1155–1167.
657 Goldstein, R.H., and Reynolds, T.J. (1994) Systematics of fluid inclusions in diagenetic
658 minerals. Society for Sedimentary Geology. Short Course, 31, 199 p.

Hoeve, J., and Quirt, D.H. (1984) Mineralization and host rock alteration in relation to clay mineral diagenesis and evolution of the Middle-Proterozoic Athabasca basin, northern Saskatchewan, Canada. Saskatchewan Research Council Technical Report 187: 187p.

Hoeve, J., and Sibbald, T.I.I. (1978) On the Genesis of Rabbit Lake and Other Unconformity-type Uranium Deposits in Northern Saskatchewan, Canada. Economic Geology, 73, 1450–1473.

IAEA (2016) World distribution of uranium deposits (UDEPO). IAEA-TECDOC-1843, 247 p.

Jefferson, C.W., Thomas, D.J., Gandhi, S.S., Ramaekers, P., Delauney, G., Brisbin, D., Cutts, C., Portella, P., and Olson, R.A. (2007) Unconformity-associated uranium deposits of the Athabasca Basin, Saskatchewan and Alberta. Bulletin of the Geological Survey of Canada, 588, 23–67.

Kerr, W. C. (2010) The discovery of the Phoenix deposit: A new high-grade, Athabasca Basin unconformity type uranium deposit, Saskatchewan, Canada. SEG Special Publication, 15, 703–728.

Komninou, A., and Sverjensky, D.A. (1996) Geochemical modeling of the formation of an unconformity-type uranium deposit. Economic Geology, 91, 590–606.

Kyser, K., and Cuney, M. (2015) Basins and uranium and deposits, in Cuney, M., and Kyser, K., eds., Geology and Geochemistry of Uranium and Thorium Deposits, Short-Course Volume 46, Mineralogical Association of Canada, p. 225–304.

680 Kyser, T. K., Wilson, M. R., and Ruhrmann, G. (1989) Stable isotope constraints on the
681 role of graphite in the genesis of unconformity-type uranium deposits. Canadian
682 Journal of Earth Sciences, 26, 490–498.
683 Lahfid, A., Beyssac, O., Deville, E., Negro, F., Chopin, C., and Goffé, B. (2010)
684 Evolution of the Raman spectrum of carbonaceous material in low-grade
685 metasediments of the Glarus Alps (Switzerland). Terra Nova, 22, 354–360.
686 Landais P., Dubessy, J., Dereppe, J.-M., and Philp, R.P. (1993) Characterization of
687 graphite alteration and bitumen genesis in the Cigar Lake deposit (Saskatchewan,
688 Canada). Canadian Journal of Earth Science 30, 743–753.
689 Leventhal, J. S., Grauch, R. I., Threlkeld, C. N., Lichte, F. E., and Harper, C. T. (1987)
690 Unusual organic matter associated with uranium from the Claude Deposit, Cluff Lake,
691 Canada. Economic Geology, 82, 1169–1176.
692 Li, Z., Chi, G., Bethune, K.M., Thomas, D., and Zaluski, G. (2017) Structural controls on
693 fluid flow during compressional reactivation of basement faults: insights from
694 numerical modeling for the formation of unconformity-related uranium deposits in the
695 Athabasca Basin, Canada. Economic Geology, 112, 451–466.
696 Li, Z., Chi, G., Bethune, K.M., Eldursi, E., Thomas, D., Quirt, D., and Ledru, P. (2018)
697 Synchronous egress and ingress fluid flow related to compressional reactivation of
698 basement faults: the Phoenix and Gryphon uranium deposits, southeastern Athabasca
699 Basin, Saskatchewan, Canada. Mineralium Deposita, 53, 277–292.

Li, Z., Chi, G., Bethune, K.M., Eldursi, K., Quirt, D., Ledru, P., and Thomas, D. (2020) Interplay between thermal convection and compressional fault reactivation in the formation of unconformity-related uranium deposits. Mineralium Deposita, in press. https://doi.org/10.1007/s00126-020-01011-6.

Marlatt, J.L., and Kyser, T.K. (2011) Paradigmatic shifts in the uranium exploration process: knowledge brokers and the Athabasca Basin learning curve. SEG Newsletter, 84, 1–23.

Martz, P., Cathelineau, M., Mercadier, J., Boiron, M., Jaguin, J., Tarantola, A., Demacon, M., Gerbeaud, O., Quirt, D., Doney, A., and Ledru, P. (2017) C-O-H-N fluids circulations and graphite precipitation in reactivated Hudsonian shear zones during basement uplift of the Wollaston-Mudjatik Transition Zone: Example of the Cigar Lake U deposit. Lithos, 294–295, 222–245.

Martz, P., Mercadier, J., Cathelineau, M., Boiron, M., Quirt, D., Doney, A., Gerbeaud, O., De Wally, E., and Ledru, P. (2019) Formation of U-rich mineralizing fluids through basinal brine migration within basement-hosted shear zones: A large-scale study of the fluid chemistry around the unconformity-related Cigar Lake U deposit (Saskatchewan, Canada). Chemical Geology, 508, 116–143.

McCready, A.J., Annesley, I.R., Parnell, J., and Richardson, L.C. (1999) Uranium-bearing carbonaceous matter, McArthur River uranium deposit, Saskatchewan. Summary of Investigation, Saskatchewan Geological Survey, Sask Energy Mines, Misc. Rep. 99–4.2, 110–120.

721 Ng, R., Alexandre, P., Kyser, K., Cloutier, J., Abdu, Y.A., and Hawthorne, F.C. (2013)
722 Oxidation state of iron in alteration minerals associated with sandstone-hosted
723 unconformity-related uranium deposits and apparently barren alteration systems in the
724 Athabasca Basin, Canada: Implications for exploration. Journal of Geochemical
725 Exploration, 130, 22–43.
726 Pagel, M. (1975) Détermination des conditions physico-chimiques de la silicification
727 diagénétique des grès Athabasca (Canada) au moyen des inclusions fluids. Comptes
728 Rendus Série D, 280, 2301–2304.
729 Pascal, M., Ansdell, K., Annesley, I. R., Kotzer, T., and Jiricka, D. (2016a)
730 Graphite-bearing pelitic schists and their altered equivalents in the Dufferin Lake Zone,
731 south-central Athabasca Basin, Saskatchewan: Constraints on graphite formation and
732 destruction, and implications for uranium mineralization. Canadian Mineralogist, 54,
733 1459–1491.
734 Pascal, M., Boiron, M. C., Ansdell, K., Annesley, I. R., Kotzer, T., Dan, J., and Cuney, M.
735 (2016b) Fluids preserved in variably altered graphitic pelitic schists in the Dufferin
736 Lake Zone, south-central Athabasca Basin, Canada: implications for graphite loss and
737 uranium deposition. Mineralium Deposita, 51, 619–636.
738 Potter, E.G., and Wright, D.M. (2015) TGI-4 Unconformity-related uranium deposits
739 synthesis: tools to aid deep exploration and refine the genetic Model. In: Targeted
740 Geoscience Initiative 4: unconformity-related uranium systems, (ed.) E.G. Potter and

741 D.M. Wright; Geological Survey of Canada, Open File 7791, p. 1–13.
742 doi:10.4095/295776

743 Rabiei, M., Chi, G., Normand, C., Davis, W.J., Fayek, M., and Blamey, N. (2017)
744 Hydrothermal REE (xenotime) mineralization at Maw Zone, Athabasca Basin, Canada,
745 and its relationship with unconformity-related uranium deposits. Economic Geology,
746 112, 1483–1507.

747 Rabiei, M., Chi, G., Potter, E.G., Tschirhart, V., MacKay, C., Frostad, S., McElroy, R.,
748 Ashley, R., McEwan, B. (2021) Fluid evolution along the Patterson Lake corridor in
749 the southwestern Athabasca Basin: constraints from fluid inclusions and implications
750 for unconformity-related uranium mineralization. Geochemistry: Exploration,
751 Environment, Analysis, DOI: https://doi.org/10.1144/geochem2020-029.

752 Ramaekers, P., Jefferson, C.W., Yeo, G.M., Collier, B., Long, D.G.F., Drever, G.,
753 McHardy, S., Jiricka, D., Cutts, C., Wheatley, K., Catuneanu, O., Bernier, S., Kupsch,
754 B., and Post, R.T. (2007) Revised geological map and stratigraphy of the Athabasca
755 Group, Saskatchewan and Alberta. Geological Survey of Canada Bulletin, 588,
756 155–191.

757 Richard, A. (2017) Radiolytic (H_2, O_2) and other trace gases (CO_2, CH_4, C_2H_6, N_2) in
758 fluid inclusions from unconformity-related U deposits. Procedia Earth and Planetary
759 Science, 17, 273–276.

760 Richard, A., Cathelineau, M., Boiron, M.-C., Mercadier, J., Banks, D.A., and Cuney, M.
761 (2016) Metal-rich fluid inclusions provide new insights into unconformity-related U

762 deposits (Athabasca Basin and Basement, Canada). Mineralium Deposita, 51,
763 249–270.
764 Roscoe, W. (2014) Technical report on a mineral resource estimate update for the
765 Phoenix uranium deposits; Wheeler River project, Eastern Athabasca Basin, Northern
766 Saskatchewan, Canada. NI 43-101 technical report prepared for Denison Mines Corp.,
767 by Roscoe Postle Associates Inc., 134 p.
768 Setzmann, U., and Wagner, W. (1991) A new equation of state and tables of
769 thermodynamic properties for methane covering the range from the melting line to 625
770 K at pressures up to 100 MPa. Journal of Physical and Chemical Reference Data, 20,
771 1061–1155.
772 Sibson, R.H. (1987) Earthquake rupturing as a mineralizing agent in hydrothermal
773 systems. Geology, 15, 701–704.
774 Sibson, R.H. (2001) Seismogenic framework for hydrothermal transport and ore
775 deposition. Reviews in Economic Geology, 14, 25–50.
776 Sibson, R.H., Robert, F., and Poulsen, K.H. (1988). High angle reverse faults, fluid
777 pressure cycling, and mesothermal gold-quartz deposits. Geology, 16, 551–555.
778 Vanderbroucke, M., and Largeau, C. (2007) Kerogen origin, evolution and structure.
779 Organic Geochemistry, 38, 719–833.
780 Wang, K. (2016) A study of petrography, fluid inclusions and graphite alteration of the
781 Phoenix uranium deposit, Athabasca Basin, northern Saskatchewan, Canada.
782 Unpublished M.Sc. thesis, University of Regina, 249 p.

783 Wang, A., Dhamenincourt, P., Dubessy, J., Guerard, D., Landais, P., and Lelaurain, M.
784 (1989) Characterization of graphite alteration in an uranium deposit by micro-Raman
785 spectroscopy, X-ray diffraction, transmission electron microscopy and scanning
786 electron microscopy. Carbon, 27, 209–218.
787 Wang, K., Chi, G., Bethune, K. M., Li, Z., Blamey, N., Card, C., Potter, E. G., and Liu, Y.
788 (2018) Fluid P-T-X characteristics and evidence for boiling in the formation of the
789 Phoenix uranium deposit (Athabasca Basin, Canada): Implications for
790 unconformity-related uranium mineralization mechanisms. Ore Geology Reviews, 101,
791 122–142.
792 Wilson, N., Stasiuk, L., and Fowler, M. (2007) Origin of organic matter in the
793 proterozoic athabasca basin of saskatchewan and alberta, and significance to
794 unconformity uranium deposits. Bulletin of the Geological Survey of Canada, 588,
795 325–339.
796 Yeo, G.M., and Delaney, G. (2007) The Wollaston Supergroup, stratigraphy and
797 metallogeny of a Paleoproterozoic Wilson cycle in the Trans-Hudson Orogen,
798 Saskatchewan Bulletin of the Geological Survey of Canada, 588, 89–117.
799 Yeo, G.M. and Potter, E.G. (2010) Review of reducing mechanisms potentially involved
800 in the formation of unconformity-type uranium deposits and their relevance to
801 exploration. Saskatchewan Geological Survey, Sask. Ministry of Energy and
802 Resources, Misc. Rep, 12, 13p.
803

This is the peer-reviewed, final accepted version for American Mineralogist, published by the Mineralogical Society of America.
The published version is subject to change. Cite as Authors (Year) Title. American Mineralogist, in press.
DOI: https://doi.org/10.2138/am-2022-8158. http://www.minsocam.org/

804 **Captions of Figures**

805 Figure 1. Maps and cross section showing the locations of samples from the Phoenix
806 uranium deposit used in this study. a) Location of the Athabasca Basin in Canada and
807 the location of the Phoenix deposit in the Athabasca Basin (modified from Card et al.
808 2007); b) Basement geology of the Phoenix deposit (modified from Roscoe 2014); the
809 insert shows the locations (collar) of diamond drill holes examined in this study; c)
810 Schematic cross section of the Phoenix deposit and neighboring areas (modified from
811 Arseneau and Revering 2010). Note the mineralized zone lies above the graphitic
812 metapelite unit in the basement; it is mainly hosted in the sandstone above the
813 unconformity, but its lower part extends into the basement. Sandstone units: Rd =
814 Read Formation, MF = Manitou Falls Formations: MFb = Bird Member, MFc =
815 Collins Member, MFd = Dunlop Member. Note the mineralized zone lies above the
816 graphitic metapelite unit in the basement; it is mainly hosted in the sandstone above
817 the unconformity, but its lower part extends into the basement. Modified from Wang et
818 al. (2018).

819 Fig. 2. Photographs of drill cores showing: a) massive uraninite overlying graphitic
820 metapelite in the basement; the orebody is surrounded by altered sandstone above and
821 altered basement rocks below, and the lower boundary of the orebody coincide with the
822 unconformity surface; b) graphitic metapelite with pervasive graphite (Gr1) crosscut by
823 graphite in a fracture (Gr3?); c) graphic metapelite with dispersed graphite (Gr1)
824 crosscut by a quartz vein which is cut by relatively coarse graphite (Gr3); d) graphite

825 (Gr3) occurring in fractures that crosscut pegmatite.

826 Fig. 3. Photomicrographs showing occurrences of different generations of graphite and
827 their features. a) flaky graphite (Gr1) in graphitic metapelite far from the unconformity;
828 b) graphite in metapelite (Gr1) showing equant shape and dissolution features in a
829 sample close to the unconformity; c) flaky graphite (Gr1) showing variable reflectance;
830 d) micro-pits in flaky graphite (Gr1) in metapelite; e) blebs of graphite (Gr2) occurring
831 as inclusions in replacement quartz in a metapelite; the insert is a bleb of Gr2 showing
832 homogeneous reflectance; f) graphite occurring in fractures (Gr3) associated with pyrite;
833 g) amorphous carbonaceous matter (Gr4) occurring in growth zones in drusy quartz; h)
834 a mineralized graphitic metapelite from the Gryphon Zone showing that graphite (Gr1)
835 and uraninite occur close to each other (< 1 mm) but generally not in contact (except
836 minor touch at the lower left corner and middle right). Note a, b and e are in transmitted
837 light, and the rest are in reflected light.

838 Fig. 4. Raman spectra of different generations of graphite (in the first order region). a) Gr1
839 showing only the G band or G band with D1 and D2 bands; b) comparison between Gr1
840 graphite with micro-pits and Gr1 without micro-pits; c) comparison between a hollow
841 point and area near the hollow point in Gr1; d) Gr2 showing only the G band without
842 discernable D bands; e) Gr3 showing only the prominent G band with or without a
843 minor D1 band; f) Gr4 showing a broad G band and a significant D1 band.

844 Fig. 5. a) occurrences of rounded graphite (Gr2) with or without a visible fluid phase,
845 which shows Raman peaks of CO_2, CH_4, and N_2; note the bump at the base of the CH_4

peak may be related to unrecognized hydrocarbons, whereas the shoulder to the right of the bump could be caused by epoxy; b) a rounded graphite (Gr2) without a visible fluid phase showing Raman peaks of CH_4 and N_2; note the sharp peak at 2918 may look like a cosmic ray effect, but its occurrence in other Gr2 grains suggests that it is not related to cosmic ray; c) occurrence of CH_4 and aqueous inclusions with rounded graphite (Gr2) in the same fluid inclusion assemblage (FIA) in a healed fracture; d) a CH_4 inclusion that shows only one phase (vapor) at room temperature and two phases (liquid and vapor) at -185^{o}C.

Fig. 6. Diagrams showing graphite contents (vol.%) versus distance from the unconformity. No significant trend is discernable, especially if the top 10 m is excluded. See text for discussion.

Fig. 7. Diagrams showing various Raman spectra parameters (D1/G, D/G, RA1 and R2, all as area ratios) indicating degree of structural disorder of graphite versus distance from the unconformity. No significant trend is discernable except for more scattered distribution toward the unconformity surface. See text for discussion.

Fig. 8. Diagrams showing D1/G area ratios of Raman spectra of graphite indicating degree of disorder versus distance from the unconformity. No significant trend is discernable. See text for discussion.

Fig. 9. Diagrams showing temperatures calculated from graphite thermometer (Beyssac et al. 2002) versus distance from the unconformity. No significant trend is discernable except for a few relatively low temperatures in the top ~25 m to the unconformity. See

867 text for discussion.

868 Fig. 10. A schematic model illustrating the genetic relationship between a graphic
869 basement fault and URU mineralization. Basement fluids enriched in reducing gases are
870 stored at depth (below ~5 km from the unconformity or ~8 km from the surface). During
871 seismic activity, the basement fluids were tapped by the reactivated fault and delivered
872 to the upper part of the fault near the unconformity. Fluid flow was controlled by the
873 'fault-valve' mechanism at the base of the fault, where fluid pressure fluctuates between
874 lithostatic and hydrostatic values, and by the 'suction pump' mechanism at the top of the
875 fault, where fluid pressure fluctuates between hydrostatic and sub-hydrostatic (Sibson
876 1987, 2001; Sibson et al. 1988). During inter-seismic periods, the enhanced
877 permeability of the fault zones allows continuous drainage of the basement fluids for a
878 certain period of time (Li et al. 2020). Uranium mineralization resulted from mixing of
879 oxidizing, U^{6+}-rich basinal brines with reducing basement fluids near the unconformity.
880 These seismic - interseismic processes were repeated multiples to form a uranium
881 deposit.

882

883 **Captions of Tables**

884 **Table 1** Contents and parameters indicating the degree of disorder of graphite (Gr1)
885 calculated from Raman spectra of samples from the Phoenix uranium deposit.

886

This is the peer-reviewed, final accepted version for American Mineralogist, published by the Mineralogical Society of America.
The published version is subject to change. Cite as Authors (Year) Title. American Mineralogist, in press.
DOI: https://doi.org/10.2138/am-2022-8158. http://www.minsocam.org/

Table 1. Contents and Raman spectroscopic characteristics of graphite of samples from the Phoenix U deposit*

Sample #	Depth (m)	Distance to u/c (m)	Graphite content (%)	D1/G		D/G		RA1**		R2**		T (°C)***
				avg.	std.	avg.	std.	avg.	std.	avg.	std.	avg.
Drill core WR-328 (dip angle 80°)												
14kw-9	375.1	3.5	1.2	0.296	0.163	0.357	0.218	0.206	0.087	0.207	0.087	549
14kw-10	376.7	5.1	2.8	0.314	0.170	0.360	0.244	0.218	0.096	0.219	0.096	544
14kw-11	378.2	6.6	2.4	0.276	0.234	0.359	0.393	0.182	0.089	0.182	0.090	560
14kw-12	381.5	9.8	4.4	0.211	0.090	0.246	0.111	0.165	0.056	0.165	0.056	568
14kw-13	384.0	12.3	4.8	0.148	0.091	0.162	0.101	0.121	0.068	0.122	0.068	587
14kw-14	385.4	13.7	5.6	0.144	0.086	0.164	0.107	0.119	0.063	0.120	0.064	588
14kw-15	386.9	15.2	6.4	0.143	0.081	0.159	0.092	0.119	0.062	0.119	0.062	588
14kw-16	388.4	16.6	7.6	0.155	0.120	0.172	0.129	0.123	0.085	0.123	0.085	586
14kw-17	389.7	17.9	5.2	0.073	0.065	0.081	0.070	0.064	0.054	0.064	0.054	613
14kw-18	391.2	19.4	9.2	0.107	0.095	0.118	0.103	0.089	0.071	0.089	0.071	601
14kw-19	392.7	20.8	4.8	0.118	0.075	0.197	0.093	0.095	0.051	0.095	0.052	599
14kw-20	394.2	22.3	4.8	0.151	0.081	0.241	0.097	0.117	0.053	0.118	0.053	588
14kw-21	395.5	23.6	0.4	0.120	0.088	0.205	0.100	0.095	0.059	0.095	0.059	588
14kw-22	397.0	25.1	5.6	0.091	0.083	0.146	0.095	0.076	0.063	0.076	0.063	607
14kw-23	398.4	26.5	3.6	0.099	0.087	0.123	0.105	0.083	0.068	0.083	0.068	604
14kw-24	400.0	28.1	2.8	0.206	0.126	0.263	0.139	0.156	0.080	0.156	0.081	572
Drill core WR-267 (dip angle 80°)												
14kw-48	414.1	3.9	2.4	0.221	0.157	0.240	0.160	0.166	0.094	0.167	0.094	567
14kw-49	417.0	6.8	4.0	0.123	0.099	0.132	0.099	0.102	0.074	0.102	0.074	596
14kw-50	420.7	10.4	6.0	0.238	0.144	0.249	0.145	0.180	0.095	0.181	0.095	560
14kw-51	423.8	13.5	4.8	0.381	0.170	0.461	0.180	0.250	0.094	0.252	0.095	529
14kw-52	428.6	18.2	8.4	0.194	0.175	0.242	0.230	0.142	0.089	0.143	0.090	577
14kw-53	433.0	22.6	4.0	0.253	0.140	0.292	0.160	0.186	0.085	0.186	0.086	558
14kw-54	443.5	32.9	0.4	-	-	-	-	-	-	-	-	-
14kw-55	453.2	42.4	4.8	0.190	0.159	0.245	0.197	0.148	0.089	0.149	0.089	575
Drill core WR-249 (dip angle 80°)												
14kw-37	425.4	15.2	1.6	0.194	0.123	0.215	0.132	0.151	0.082	0.151	0.082	574
14kw-38	434.9	24.6	0.8	0.197	0.155	0.263	0.166	0.144	0.103	0.144	0.103	577
14kw-39	438.7	28.4	2.4	0.101	0.094	0.116	0.103	0.084	0.069	0.085	0.069	603
14kw-40	438.9	28.6	3.6	-	-	-	-	-	-	-	-	-
14kw-41	446.5	36.0	6.0	0.221	0.189	0.245	0.207	0.163	0.098	0.163	0.099	568
14kw-42	452.6	42.1	3.2	0.155	0.117	0.170	0.121	0.124	0.083	0.124	0.083	586
14kw-43	459.3	48.6	6.4	0.128	0.123	0.153	0.127	0.102	0.090	0.102	0.090	596
Drill core WR-444 (dip angle 90°)												
14kw-57	417.9	15.2	0.0	-	-	-	-	-	-	-	-	-
14kw-58	431.9	29.2	1.2	0.174	0.108	0.248	0.128	0.133	0.069	0.134	0.070	581
14kw-59	435.9	33.2	1.6	0.112	0.091	0.184	0.110	0.089	0.066	0.090	0.067	601
14kw-60	442.9	40.2	4.4	0.187	0.129	0.204	0.136	0.146	0.090	0.146	0.090	576
14kw-61	447.6	44.9	6.4	0.133	0.116	0.148	0.121	0.107	0.084	0.107	0.084	593
14kw-62	457.0	54.3	1.6	0.155	0.098	0.174	0.114	0.126	0.066	0.126	0.066	585
14kw-63	471.9	69.2	2.0	0.283	0.165	0.325	0.184	0.201	0.096	0.201	0.096	552
Drill core WR-498 (dip angle 90°)												
14kw-67	418.6	14.0	1.2	0.170	0.133	0.189	0.140	0.133	0.087	0.133	0.087	582
14kw-68	424.3	19.7	6.4	0.181	0.133	0.208	0.149	0.140	0.085	0.141	0.085	578
14kw-69	426.0	21.4	0.8	0.428	0.217	0.460	0.236	0.279	0.098	0.280	0.098	516
Drill core WR-412 (dip angle 75°)												
14kw-73	398.5	17.8	1.6	0.343	0.222	0.368	0.233	0.231	0.124	0.232	0.124	538
14kw-74	564.9	178.5	2.4	0.199	0.141	0.225	0.145	0.152	0.088	0.153	0.088	573
14kw-75	518.9	134.1	7.6	0.158	0.103	0.201	0.113	0.125	0.071	0.126	0.071	585
14kw-76	519.9	135.0	0.8	-	-	-	-	-	-	-	-	-

* Most samples are from the graphitic metapelite – SW Shear Zone except those in the shaded rows, which are from the hanging wall and footwall of the SW Shear Zone (those from drill core WR-412 are ~500 m to the west of the SW Shear Zone)

** RA1=(D1+D4) / (D1+D2+D3+D4+G) area ratio according to Lahfid et al. (2010); R2=D1 / (G+D1+D2) area ratio according to Beyssac et al. (2002)

*** T (°C) = -445 R2 + 641 according to Beyssac et al. (2002)

This is the peer-reviewed, final accepted version for American Mineralogist, published by the Mineralogical Society of America.
The published version is subject to change. Cite as Authors (Year) Title. American Mineralogist, in press.
DOI: https://doi.org/10.2138/am-2022-8158. http://www.minsocam.org/

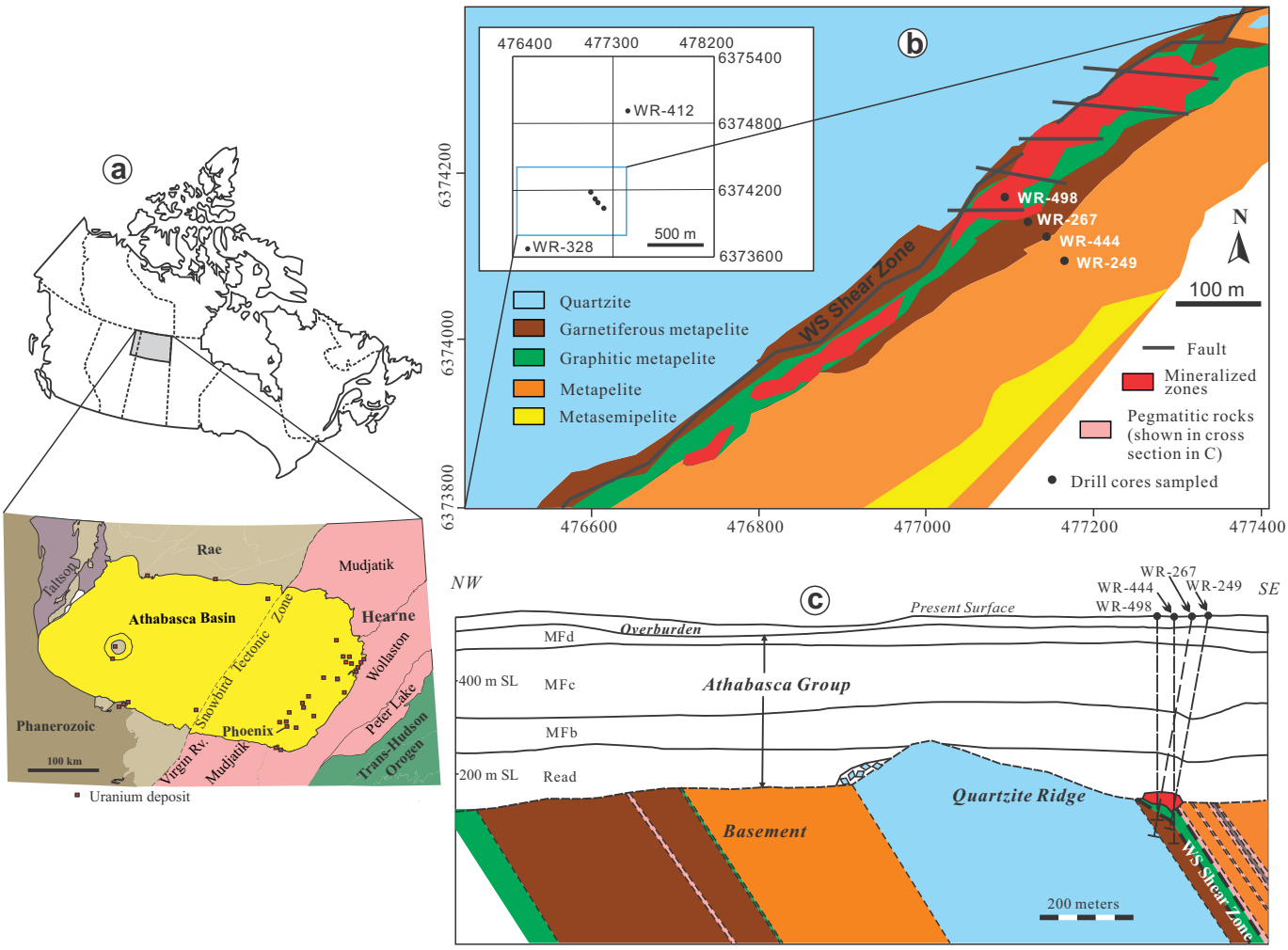

Songg et al Fig 1

This is the peer-reviewed, final accepted version for American Mineralogist, published by the Mineralogical Society of America.
The published version is subject to change. Cite as Authors (Year) Title. American Mineralogist, in press.
DOI: https://doi.org/10.2138/am-2022-8158. http://www.minsocam.org/

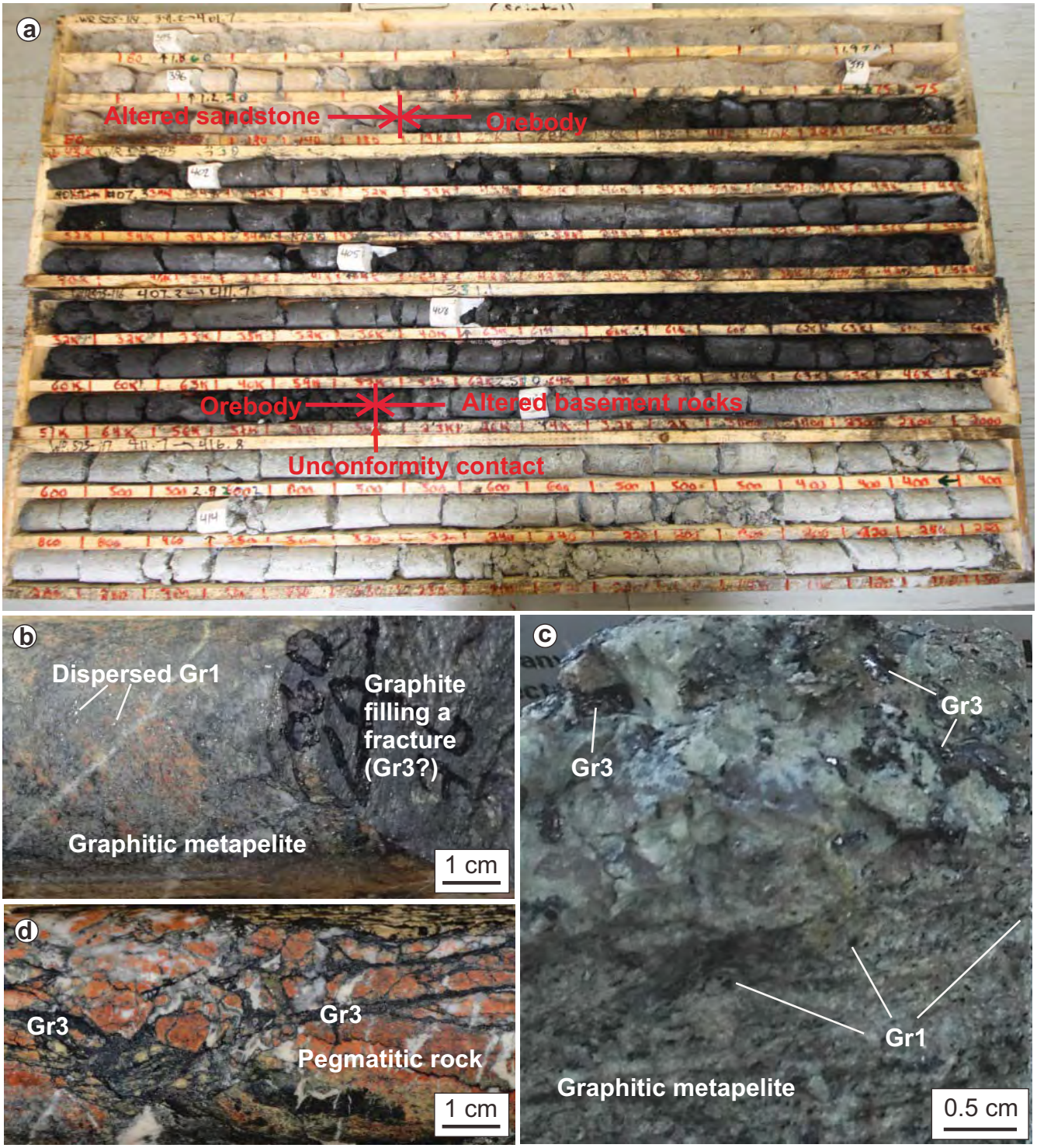

Song et al. Fig. 2

This is the peer-reviewed, final accepted version for American Mineralogist, published by the Mineralogical Society of America.
The published version is subject to change. Cite as Authors (Year) Title. American Mineralogist, in press.
DOI: https://doi.org/10.2138/am-2022-8158. http://www.minsocam.org/

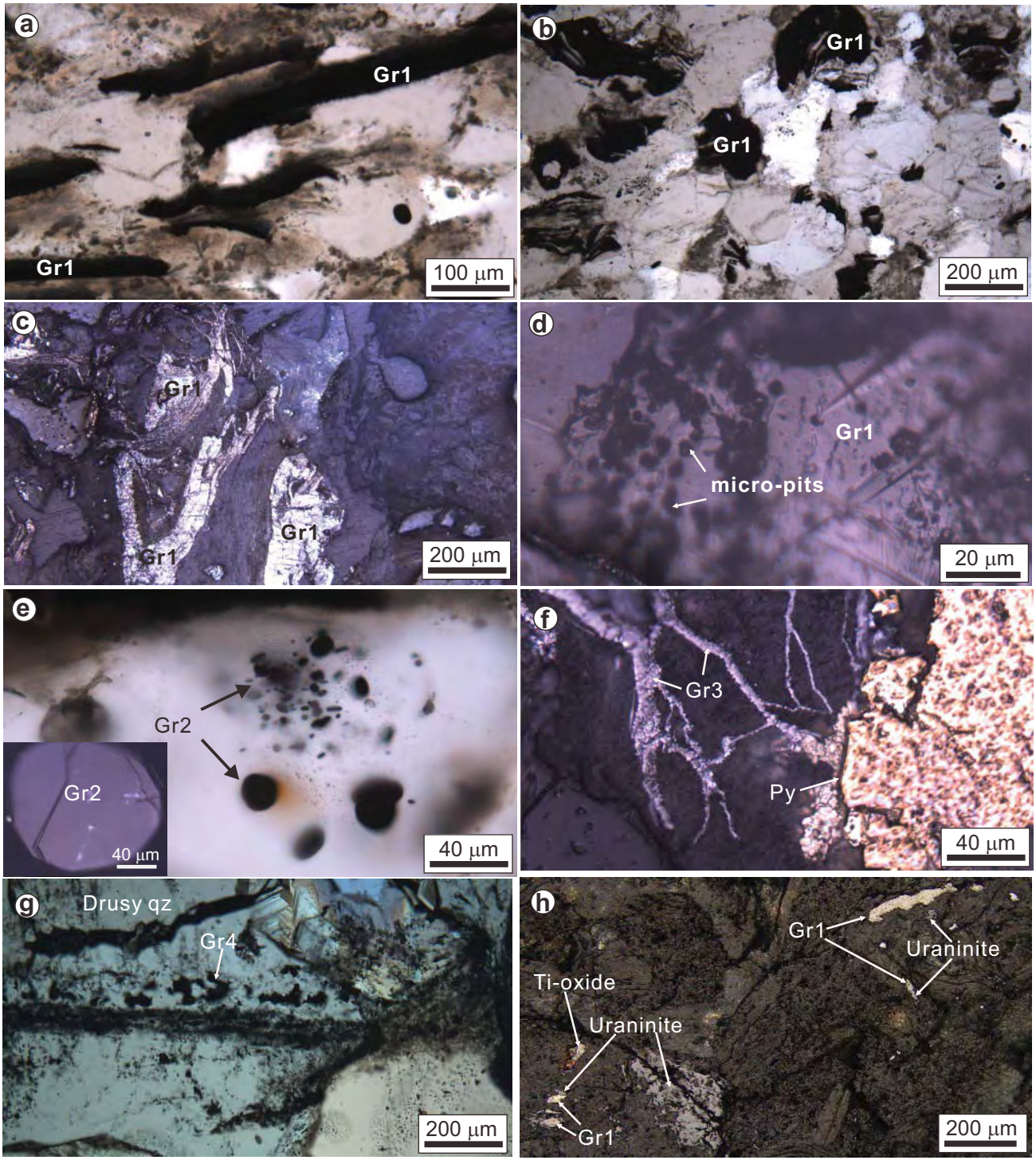

Song et al. Fig. 3

This is the peer-reviewed, final accepted version for American Mineralogist, published by the Mineralogical Society of America.
The published version is subject to change. Cite as Authors (Year) Title. American Mineralogist, in press.
DOI: https://doi.org/10.2138/am-2022-8158. http://www.minsocam.org/

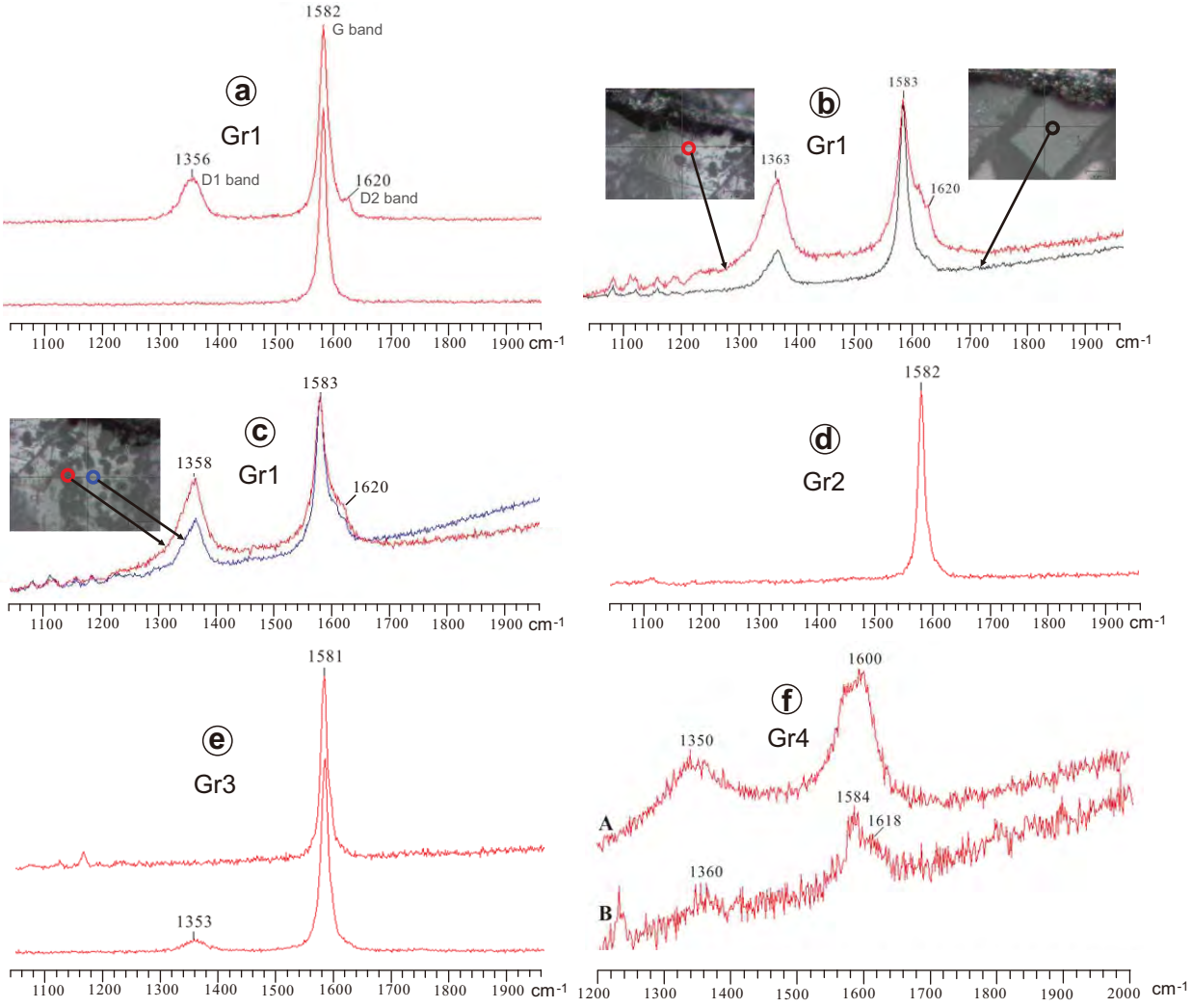

Song et al. Fig. 4

This is the peer-reviewed, final accepted version for American Mineralogist, published by the Mineralogical Society of America.
The published version is subject to change. Cite as Authors (Year) Title. American Mineralogist, in press.
DOI: https://doi.org/10.2138/am-2022-8158. http://www.minsocam.org/

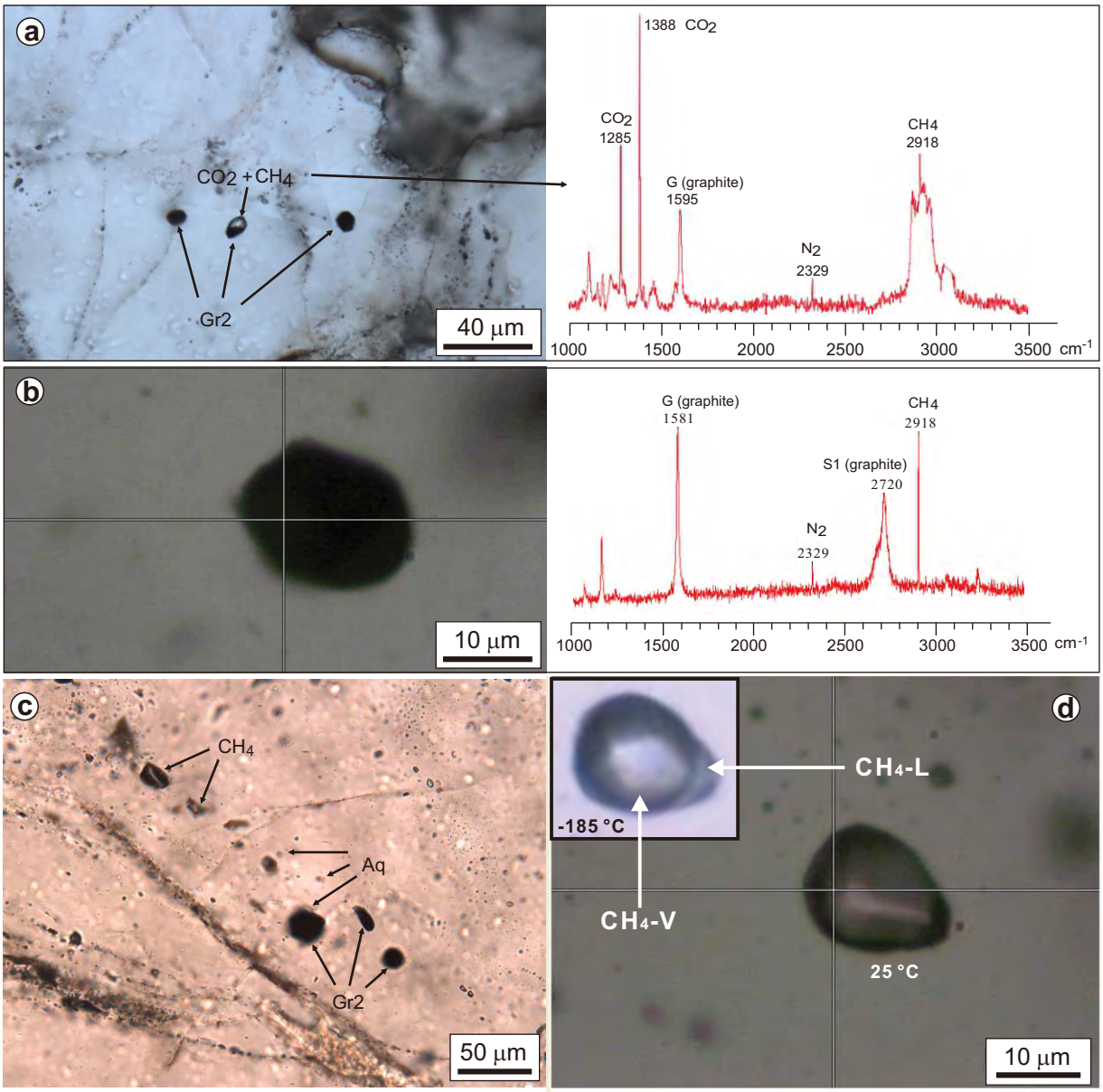

Song et al Fig. 5

This is the peer-reviewed, final accepted version for American Mineralogist, published by the Mineralogical Society of America.
The published version is subject to change. Cite as Authors (Year) Title. American Mineralogist, in press.
DOI: https://doi.org/10.2138/am-2022-8158. http://www.minsocam.org/

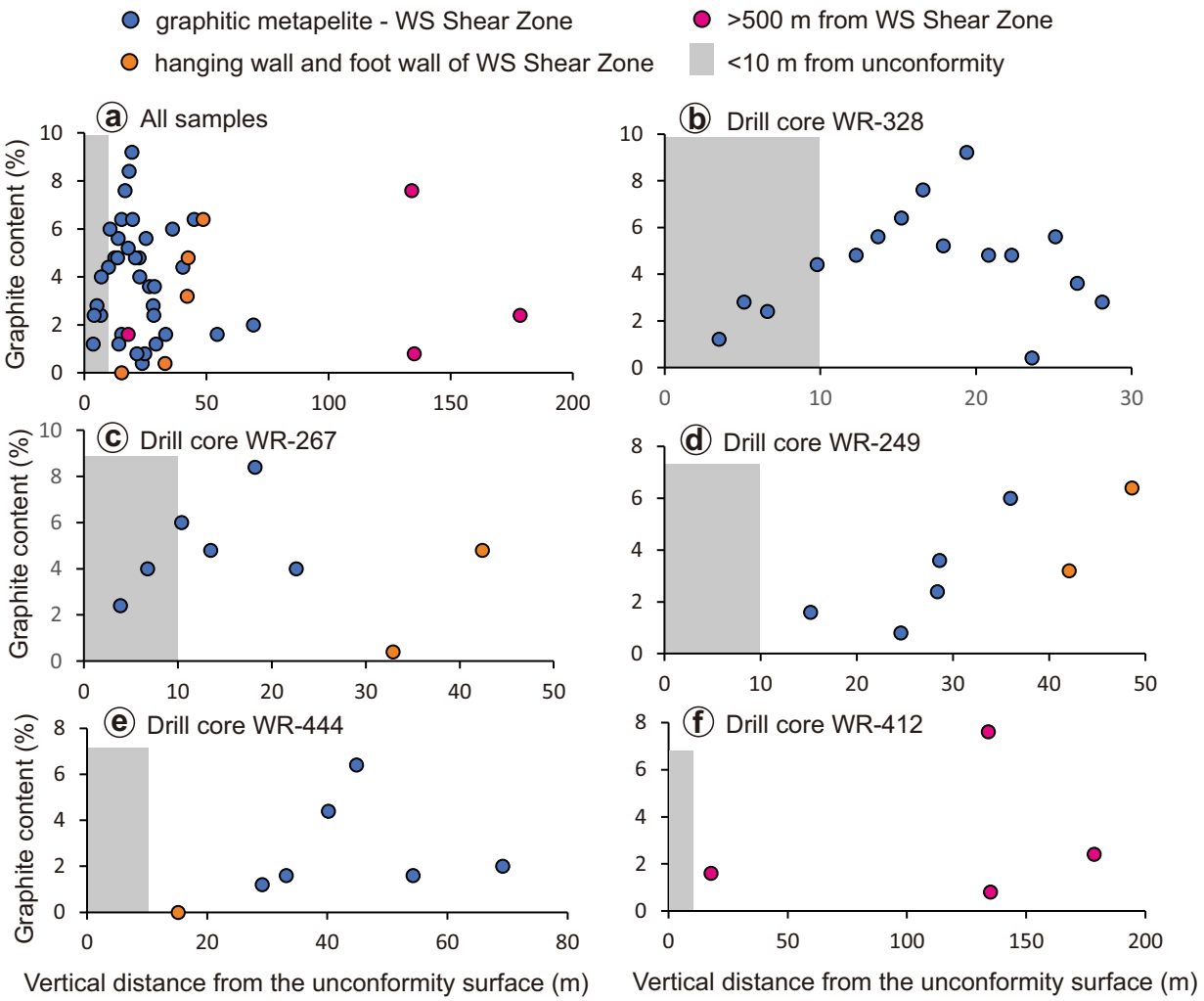

Song et al. Fig. 6

This is the peer-reviewed, final accepted version for American Mineralogist, published by the Mineralogical Society of America.
The published version is subject to change. Cite as Authors (Year) Title. American Mineralogist, in press.
DOI: https://doi.org/10.2138/am-2022-8158. http://www.minsocam.org/

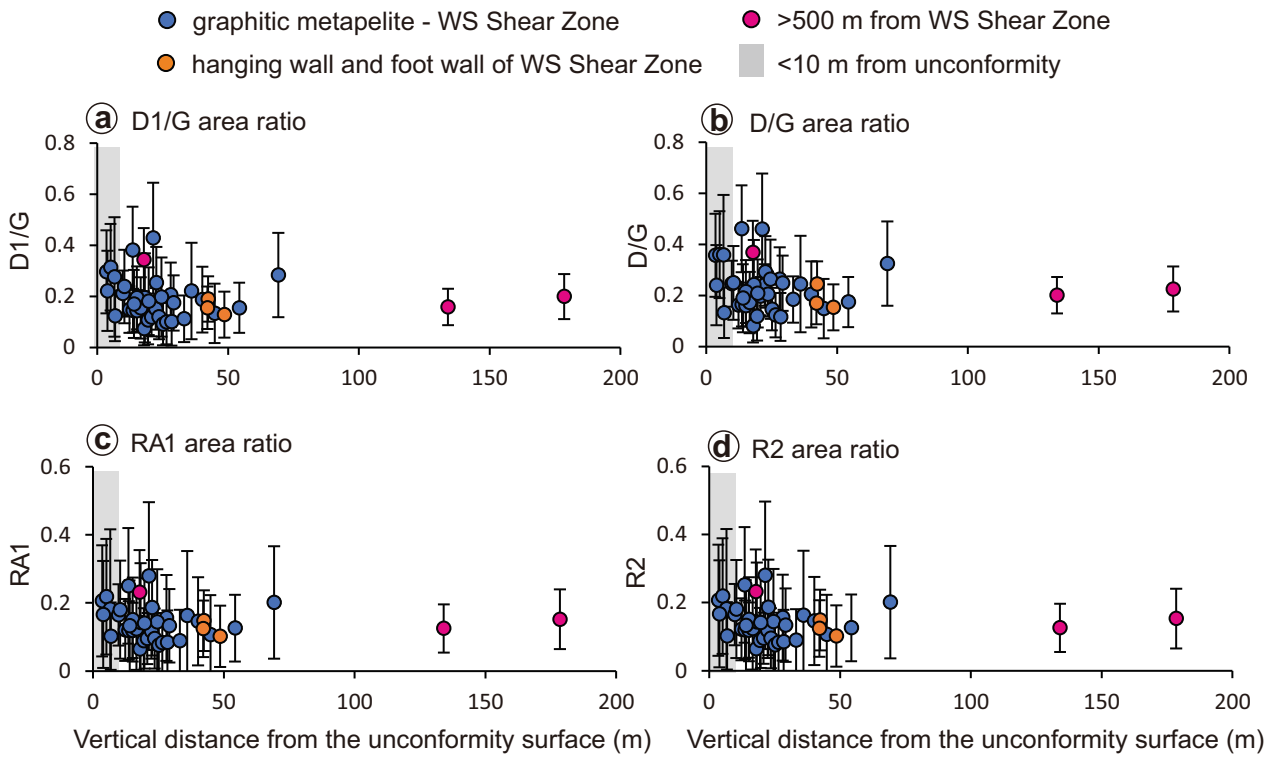

Song et al. Fig. 7

This is the peer-reviewed, final accepted version for American Mineralogist, published by the Mineralogical Society of America.
The published version is subject to change. Cite as Authors (Year) Title. American Mineralogist, in press.
DOI: https://doi.org/10.2138/am-2022-8158. http://www.minsocam.org/

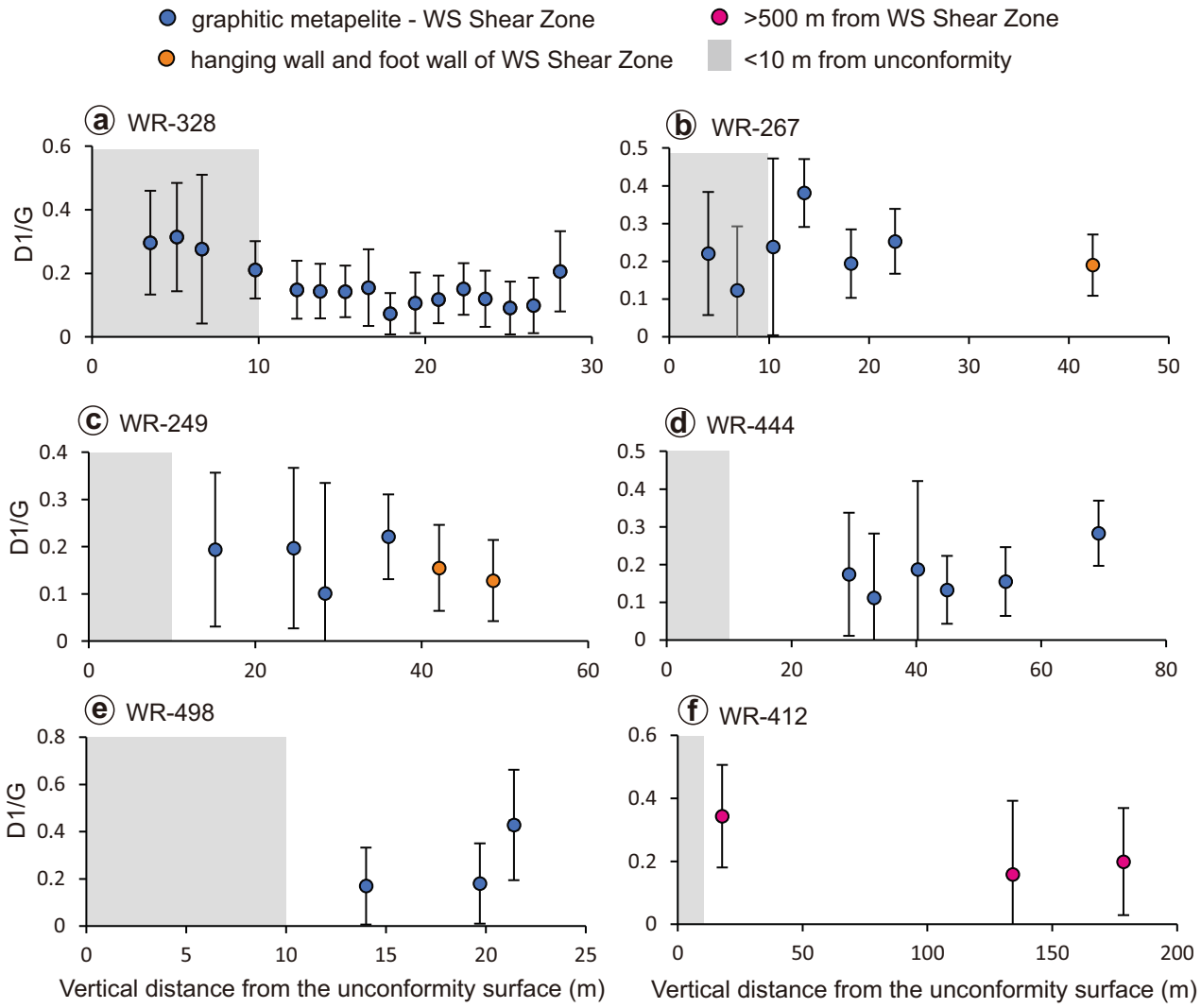

Song et al. Fig. 8

This is the peer-reviewed, final accepted version for American Mineralogist, published by the Mineralogical Society of America.
The published version is subject to change. Cite as Authors (Year) Title. American Mineralogist, in press.
DOI: https://doi.org/10.2138/am-2022-8158. http://www.minsocam.org/

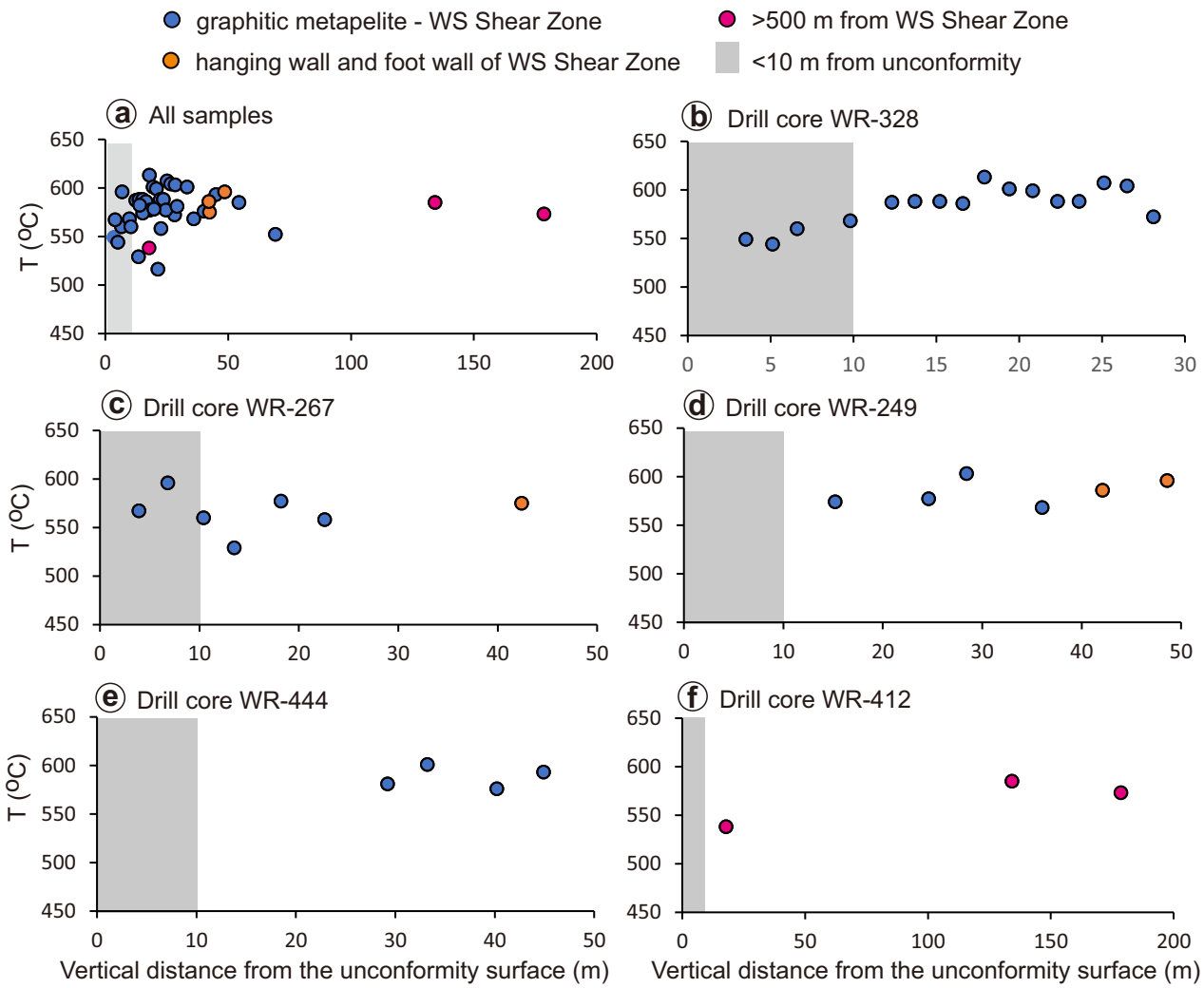

Song et al. Fig. 9

This is the peer-reviewed, final accepted version for American Mineralogist, published by the Mineralogical Society of America.
The published version is subject to change. Cite as Authors (Year) Title. American Mineralogist, in press.
DOI: https://doi.org/10.2138/am-2022-8158. http://www.minsocam.org/

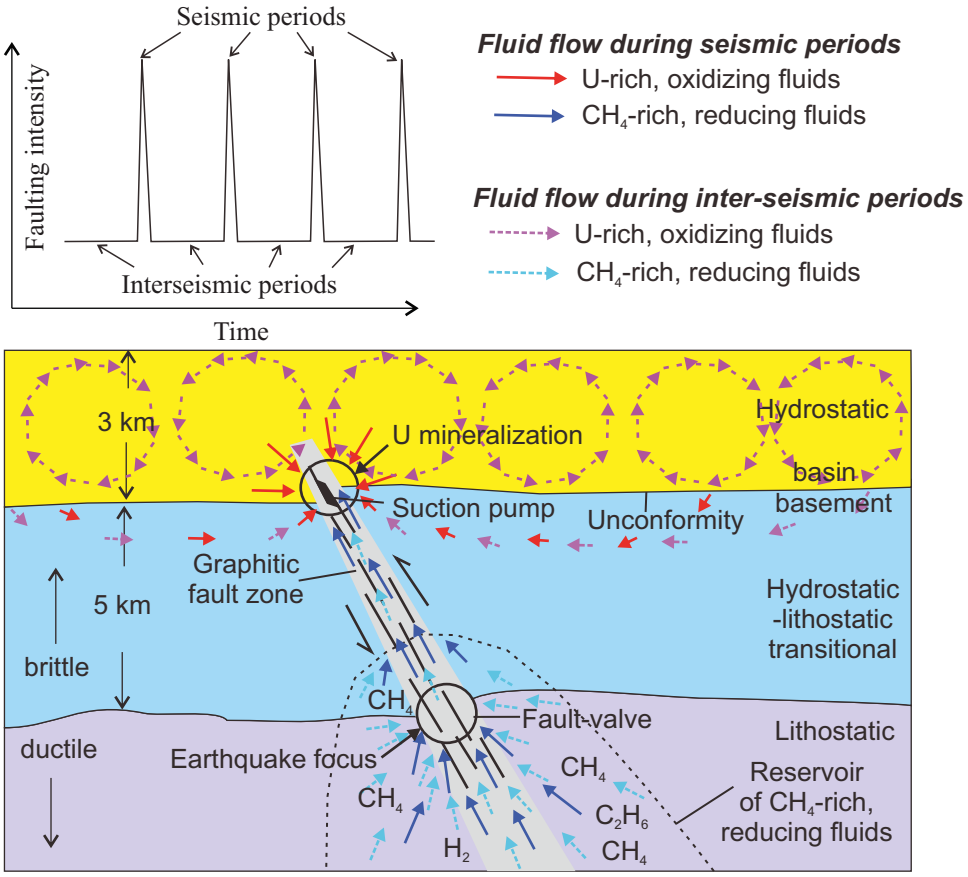

Song et al. Fig. 10